Dynamical downscaling: Assessment of value retained and added using the Regional Atmospheric Modeling System (RAMS)

Christopher L. Castro, Roger A. Pielke Sr., and Giovanni Leoncini
Department of Atmospheric Science, Colorado State University, Fort Collins, Colorado, USA

Received 1 March 2004; revised 29 October 2004; accepted 10 December 2004; published 11 March 2005.

[1] The value restored and added by dynamical downscaling is quantitatively evaluated by considering the spectral behavior of the Regional Atmospheric Modeling System (RAMS) in relation to its domain size and grid spacing. A regional climate model (RCM) simulation is compared with NCEP Reanalysis data regridded to the RAMS grid at each model analysis time for a set of six basic experiments. At large scales, RAMS underestimates atmospheric variability as determined by the column integrated kinetic energy and integrated moisture flux convergence. As the grid spacing increases or domain size increases, the underestimation of atmospheric variability at large scales worsens. The model simulated evolution of the kinetic energy relative to the reanalysis regridded kinetic energy exhibits a decrease with time, which is more pronounced with larger grid spacing. Additional follow-on experiments confirm that the surface boundary forcing is the dominant factor in generating atmospheric variability for small-scale features and that it exerts greater control on the RCM solution as the influence of lateral boundary conditions diminish. The sensitivity to surface forcing is also influenced by the model parameterizations, as demonstrated by using a different convection scheme. For the particular case considered, dynamical downscaling with RAMS in RCM mode does not retain value of the large scale which exists in the larger global reanalysis. The utility of the RCM, or value added, is to resolve the smaller-scale features which have a greater dependence on the surface boundary. This conclusion regarding RAMS is expected to be true for other RCMs as well.

Citation: Castro, C. L., R. A. Pielke Sr., and G. Leoncini (2005), Dynamical downscaling: Assessment of value retained and added using the Regional Atmospheric Modeling System (RAMS), *J. Geophys. Res.*, *110*, D05108, doi:10.1029/2004JD004721.

1. Introduction

[2] The term "downscaling" refers to the use of either fine spatial-scale numerical atmospheric models (dynamical downscaling), or statistical relationship (statistical downscaling) in order to achieve detailed regional and local atmospheric data. The starting point for downscaling is typically a larger-scale atmospheric or coupled oceanic-atmospheric model run globally (GCM). The downscaled high resolution data can then be inserted into other types of numerical simulation tools such as hydrological, agricultural, and ecological models. This paper focuses on dynamical downscaling with a regional climate model (RCM). By RCM we mean a limited area (weather prediction) model (LAM) run for an integration time greater than approximately two weeks, so that the sensitivity to initial atmospheric conditions is lost [*Jacob and Podzun*, 1997]. A summary of dynamical downscaling is reported in chapter 10 of the 2001 Intergovernmental Panel on Climate Change (IPCC) science report. By examining a sample case with the Regional Atmospheric Modeling System (RAMS), this paper presents evidence of when downscaling may be a valid tool to enhance spatial resolution and when it is not. LAM dynamical downscaling can be classified into four distinct types:

[3] 1. Type 1: LAM forced by lateral boundary conditions from a numerical weather prediction GCM or global data reanalysis at regular time intervals (typically 6 or 12 h), by bottom boundary conditions (e.g., terrain), and specified initial conditions. A numerical weather prediction GCM is a GCM in which the global initial atmospheric conditions are not yet forgotten.

[4] 2. Type 2: LAM initial atmospheric conditions have been forgotten, but results are still dependent on the lateral boundary conditions from an NWP GCM or global data reanalysis and on the bottom boundary conditions.

[5] 3. Type 3: Lateral boundary conditions are provided from a GCM which is forced with specified surface boundary conditions.

[6] 4. Type 4: Lateral boundary conditions from a completely coupled earth system global climate model in which the atmosphere-ocean-biosphere and cryosphere are interactive.

[7] Tables 1 and 2 illustrate examples of each type of downscaled model. Table 1 overviews RCM dependence on the indicated constraints for the four types. Table 2 shows that these constraints and the predictive skill of LAMs

0148-0227/05/2004JD004721$09.00

Table 1. Dependence of Regional Model on Indicated Constraints

	Type 1	Type 2	Type 3	Type 4
Bottom boundary conditions	terrain; LDAS[a]; observed SSTs	terrain; climatological vegetation; observed SSTs; deep soil moisture	terrain; climatological vegetation; observed SSTs; deep soil moisture	terrain; soils
Initial conditions	ETA analysis field	none	none	none
Lateral boundary conditions	Global Forecast System Atmospheric Model[b]	NCEP Reanalysis[c]	global model forced by observed SSTs	IPCC[d]; U.S. National Assessment[e]
Regional	ETA[f] MM5[g] RAMS[h] ARPS[i]	PIRCS[j]	COLA[k]/ETA[l]	RegCM[m]

[a]Available at http://ldas.gsfc.nasa.gov/.
[b]Available at http://wwwt.emc.ncep.noaa.gov/gmb/moorthi/gam.html.
[c]*Kalnay et al.* [1996].
[d]*Houghton et al.* [2001].
[e]Available at http://www.gcrio.org/NationalAssessment/.
[f]*Black* [1994].
[g]*Grell et al.* [1994].
[h]*Pielke et al.* [1992].
[i]*Xue et al.* [2000, 2001].
[j]*Takle et al.* [1999].
[k]Available at http://www-pcmdi.llnl.gov/modldoc/amip/14cola.html.
[l]*Mesinger et al.* [1997].
[m]*Giorgi et al.* [1993a, 1993b].

becomes less as an attempt is made to forecast further into the future. Types 2 through 4 can be considered RCM modes.

[8] With short-term numerical weather prediction (Type 1), the observations used in the analysis to initialize a model retain a component of realism even when degraded to the coarser model resolution of a global model (i.e., the data are sampled from a continuous field). This realism persists for a period of time (up to a week or so), when used as lateral boundary conditions for a weather prediction LAM. This is not true with Type 4 simulations, where observed data does not exist to influence the predictions [*Pielke*, 2001]. LAMs cannot significantly increase predictability if the solution is highly dependent on the large-scale forcing supplied by the lateral boundaries. Even when the model solution is strongly influenced by the surface boundary, improved skill still cannot be achieved without accurate lateral boundary conditions.

[9] In this work, the value retained and value added by dynamical downscaling with a RCM is quantitatively evaluated by considering the spectral behavior of the RAMS model solution in relation to its domain size and grid spacing. By ''value retained'' we mean how well the RCM maintains fidelity with the large-scale behavior of the global model forcing data. By ''value added'' we mean how much additional information the RCM can provide beyond the highest resolved wavelength of the global model. We assume ''perfect'' bottom and lateral boundary conditions, as defined respectively by observed SSTs and atmospheric reanalyses (e.g., Type 2). Examples of Type 2 simulations include the Project to Intercompare Regional Climate Simulations (PIRCS) as reported in *Takle et al.* [1999]. In such a framework we can pose the questions: (1) what is the dependence on the evolution of synoptic features to the lateral boundary conditions, and (2) what is the most appropriate domain size and grid spacing for RCM downscaling?

[10] These questions have been previously investigated to some extent by RCM experiments which change the specification of the lateral boundaries. This may be done using a

Table 2. Examples of Predictability[a]

	Type	Constraints
Day-to-day weather prediction	1	initial conditions; lateral boundary conditions topography; other bottom land boundary conditions; solar irradiance; well-mixed greenhouse gases
Seasonal weather simulation	2	lateral boundary conditions; topography; other bottom land boundary conditions; solar irradiance; well-mixed greenhouse gases
Season weather prediction	3	topography; other bottom land boundary conditions; sea surface temperatures; solar irradiance; well-mixed greenhouse gases
Multiyear climate prediction	4	topography; solar irradiance; well-mixed greenhouse gases

[a]From top to bottom of table: more constraints to fewer constraints; from bottom to top of table: less predictive skill to greater predictive skill.

Table 3. Commonly Used Acronyms

Acronym	Meaning
AOGCM	atmosphere-ocean general circulation model
GCM	general circulation model
LAM	limited area model
MFC	integrated moisture flux convergence
NCEP	National Centers for Environmental Prediction
NSSL	National Severe Storms Laboratory
RAMS	Regional Atmospheric Modeling System
RCM	regional climate model
SST	sea surface temperature

so-called "Big Brother" approach [e.g., *de Elía et al.*, 2002; *Denis et al.*, 2002, 2003]. In these types of experiments, forcing data to a nested RCM grid (Little Brother) are spectrally degraded to eliminate small-scale variability. The results are then compared to a reference simulation (Big Brother) with no spectral degradation of the forcing. Another approach is to change the specification of the primary RCM grid itself, which is what we choose to do here. *Denis et al.* [2002] provide a good summary of studies of this type, including *Jones et al.* [1995, 1997], *Jacob and Podzun* [1997], and *Seth and Giorgi* [1998]. All of these studies note significant sensitivities to the specification of the RCM grid, as shown, for example, in precipitation and strength of mesoscale features.

[11] We extend their work with RAMS to show that, absent a means of updating the interior of the domain, the RCM cannot retain value of the large scale. We then show the value added, or skill of the RCM, is dependent on how the large scale is represented, how the surface boundary is specified, and the model physics. Section 2 describes the RAMS model and experimental methodology. Section 3 presents the results from RAMS downscaling sensitivity experiments. A discussion and summary are presented in sections 4 and 5. Tables 3 and 4 give a list of frequently used acronyms and symbols.

2. Methodology

2.1. Description of RCM

[12] The RCM used in these experiments is the Regional Atmospheric Modeling System (RAMS) Version 4.3. RAMS was originally developed at Colorado State University to facilitate research into predominately mesoscale and cloud-scale atmospheric phenomena, but has been extended to larger scales over the last decade or so [*Cotton et al.*, 2003]. This model is fully three-dimensional, nonhydrostatic; includes telescoping, interactive nested grid capabilities, supports various turbulence closure, short and long wave radiation, initialization, and boundary condition schemes [*Pielke et al.*, 1992].

[13] Two domains sizes are used in the model sensitivity experiments (Figure 1). We chose to simulate the month of May 1993 because it is a time of vigorous synoptic wave activity associated with large-scale flooding over the central United States [e.g., *Bell and Janowiak*, 1995]. The first domain covers all of the contiguous United States and is similar to a typical numerical weather forecast domain used operationally for the WRF and ETA models at the National Centers for Environmental Prediction (NCEP) and National Severe Storms Laboratory (NSSL). The second domain covers almost the entire western half of the Northern Hemisphere. A summary of the domain information and relative computational expense is shown in Table 5.

[14] Each domain is run for a horizontal grid spacing corresponding to 200, 100, and 50 km for a total of six runs which comprise the basic set of experiments. Aside of the grid spacing and domain size, all the other conditions in RAMS are uniform. The model time step is 60 s. Thirty vertical levels are used with a maximum vertical grid spacing of 1000 m. The turbulent mixing parameterization of *Mellor and Yamada* [1974] is used to compute the vertical mixing coefficients. A modified *Smagorinsky* [1963] deformation-based scheme is used to compute the horizontal mixing coefficient (or diffusion), per grid point defined as:

$$K_i = \rho_o \max\left[K_{mh}, (C_x \Delta x)^2 S_2^{0.5}\right] \quad (1)$$

where ρ_o is the basic state air density, Δx is the model grid spacing, C_x is a user-specified dimensionless coefficient to obtain a characteristic horizontal mixing length scale, and S_2 is the horizontal strain rate (a function of the horizontal winds). K_{mh} is a lower limit on the horizontal diffusion according to the empirical formula:

$$K_{mh} = 0.075 K_A \left(\Delta x^{4/3}\right) \quad (2)$$

where K_A is a user-defined parameter. The typical range of K_{mh} can be estimated by varying K_A in equation (2) from 0.1 to 1, as suggested by the RAMS Users Guide. The

Table 4. Commonly Used Symbols

Symbol	Meaning
$a_{i,j}$	RCM variable
$a_{i,j}^N$	detrended RCM variable
$c_{p,q}$	spectral coefficient of given detrended atmospheric model variable as function of zonal and meridional wavenumber
C_x	user-specified coefficient to obtain a characteristic horizontal mixing length scale
$\underline{Ek}_{i,j}$	column average total kinetic energy
$\overline{Ek}$	domain-averaged total kinetic energy
i	subscript for x-dimension of reduced RCM grid
j	subscript for y-dimension of reduced RCM grid
k	wavenumber
k^*_{max}	maximum physically resolved wavenumber of NCEP reanalysis
$k_{Nyquist}$	Nyquist wavenumber of RCM
$k^*_{Nyquist}$	Nyquist wavenumber of NCEP reanalysis
Δk	minimum wavenumber for a given RCM grid spacing
K_A	user-specified parameter used in computing lower limit of horizontal mixing coefficient
K_i	horizontal mixing (diffusion) coefficient
N_I	maximum x-dimension of reduced RCM grid
N_J	maximum y-dimension of reduced RCM grid
p	subscript for zonal wavenumber
q	subscript for meridional wavenumber
S_2	horizontal strain rate
$S(k)_{obs}$	spectral power per wavenumber of regridded reanalysis
$S(k)_{mod}$	spectral power per wavenumber of RCM simulation
$\Delta S(k)_{frac}$	fractional change in spectral power per wavenumber
Δx	RCM grid spacing
Λ	wavelength
ρ_o	basic state air density
$\overline{\sigma}^2_{EK}$	domain-averaged kinetic energy variance

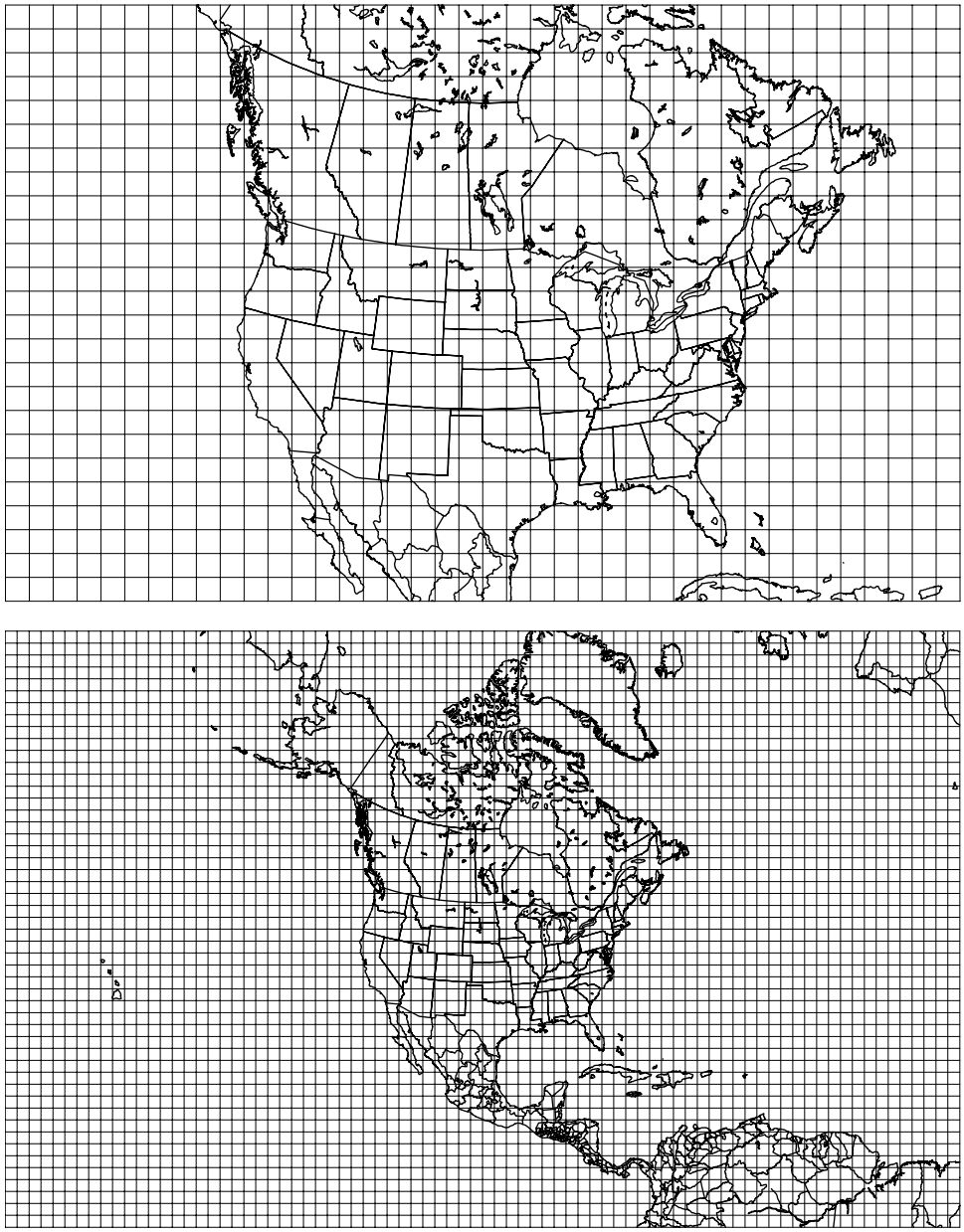

Figure 1. RAMS domains for model sensitivity experiments for Δx = 200 km.

ranges of K_{mh} for the three grid spacings used in the experiments are shown in Table 6.

[15] The model is initialized and updated at the lateral boundaries every six hours by the NCEP reanalysis at 2.5° latitude by 2.5° longitude [*Kalnay et al.*, 1996] with three nudging points at the lateral boundary. Lateral boundary nudging is according to the form of *Davies* [1976]. This common technique in LAMs is summarized by *Laprise* [2003]. The model variables are nudged to the larger-scale forcing data over a (user-defined) sponge zone of grid points, and the e-folding time varies from a short timescale near the boundary to an infinite value beyond the

Table 5. Model Domain Specifications and Computational Increase for the Six Basic Experiments[a]

Basic Experiment	Δx, km	Domain	RCM Grid Dimensions	Computational Increase
1	200	small	40 × 25	1
2	100	small	80 × 50	3.5
3	50	small	160 × 100	15.2
4	200	large	80 × 50	3.5
5	100	large	160 × 100	15.2
6	50	large	320 × 200	62.8

[a]The computational increase is computed as the time to complete one model time step for the given domain divided by that for the basic experiment 1.

Table 6. Typical Values for the Lower Limit of the Horizontal Mixing Coefficient (K_{mh}) Estimated by Equation (2)[a]

Δx, km	K_{mh}
200	$1.38 \times 10^4 - 1.38 \times 10^5$
100	$3.48 \times 10^4 - 3.48 \times 10^5$
50	$8.77 \times 10^4 - 8.77 \times 10^5$

[a]Units are in $m^2\ s^{-1}$.

sponge zone. The physical width of sponge zone does change with grid spacing, but the number of nudging points is sufficient to resolve the Nyquist wavenumber of the given LAM grid. The version of RAMS used here also has a simple four-dimensional data assimilation option to nudge the interior prognostic variables of wind, temperature, pressure (Exner function), and water vapor at a user-specified timescale, which we implement for some of the experiments discussed in section 3. The SSTs for May 1993 are from the *Reynolds and Smith* [1994] data and are constant for the month of simulation. Topography and vegetation data are from standard products in the RAMS model package. The soil type (sandy clay loam) is uniform for all land areas and the model is initialized with homogeneous soil moisture at 50% of field capacity.

[16] The simplest and most computationally expedient parameterizations were chosen for the set of basic experiments. The Kuo convection scheme [*Kuo*, 1974; *Molinari*, 1985] and *Mahrer and Pielke* [1977] radiation parameterization options are used with no explicit treatment of cloud microphysics. The convection scheme is the only mechanism in the model to produce rainfall. Otherwise, water vapor is advected or diffused in the atmosphere, even if supersaturation occurs. Buoyancy and radiative effects of water vapor are accounted for. We also used the Kain-Fritsch (KF) convection scheme [*Kain and Fritsch*, 1993] as recently implemented in RAMS by *Castro et al.* [2002] for some of the follow-on experiments described in section 3. We acknowledge that neglecting large-scale precipitation produced by supersaturation may not be physically realistic. However, we emphasize that these experiments are designed to test RCM sensitivity using the simplest and most computationally expedient parameterizations. Even when RAMS includes a large-scale condensation scheme, its warm season precipitation is mostly from convection. The effect of using an explicit microphysical representation of large-scale precipitation is considered in section 4.

[17] The nudging timescale, the number of nudging points at the lateral boundary, and other user-specified parameters, such as vertical diffusion, are held constant for all experiments according to suggested values in the RAMS Users Guide (http://www.atmet.com/html/documentation.shtml). The choice of user-defined parameters and parameterization options could be varied to see if the results from the present investigation would possibly change. However, the intent here is demonstrate the characteristics of the basic RAMS model "off the shelf" without any adjustment to suggested user specifications. The skill performance of the RAMS model in a RCM mode is reported in *Eastman et al.* [2001] and *Liston and Pielke* [2001]. Additional experiments which investigate the influence of surface boundary conditions and interior nudging are described in the results section.

[18] Data were saved twice per day at 0 UTC and 12 UTC. To determine how model variables differ from the "perfect" reanalysis model as time proceeds, the reanalysis data were vertically and horizontally interpolated to RAMS grid each day at 0 UTC and 12 UTC for all the model simulations. We treat the RAMS regridded reanalysis as the "observed" NCEP reanalysis on the given LAM grid. While this procedure may introduce errors into what we consider "perfect observations" (R. Walko, personal communication), the regridded reanalysis is very consistent with the reanalysis itself, particularly for larger-scale features. Any difference between the model output and regridded reanalysis less than the smallest wavelength resolved by the reanalysis, then, is due to the physics of the RAMS model. By "physics" we mean the dynamical core of the model and the model parameterization schemes. As in *de Elía et al.* [2002], to eliminate possible spurious values at the model lateral boundaries, the three outermost grid points were first removed from the raw model grid. The reduced grid of $N_I \times N_J$ defines the grid used henceforth in the analyses.

2.2. Two-Dimensional Spectral Analysis of Model Variables

[19] There are various methods to determine the power spectra of an atmospheric variable ($a_{i,j}$) within a LAM domain. As summarized by *Laprise* [2003], the earliest and most straightforward method is that of *Errico* [1985] which uses a double Fourier series after removing a linear trend in each direction. Other approaches which also remove a trend in the RCM domain include those of *Tatsumi* [1986] and *Chen and Kuo* [1992]. *Denis et al.* [2002] recently used double cosine transforms to spectrally analyze LAM fields without subtracting any component. We choose to use *Errico*'s [1985] method here for its simplicity, but we are mindful of the caveats, as discussed, for example, in *Denis et al.* [2002]. Detrending removes the large-scale gradient across the LAM domain, which may affect the large-scale components of the spectrum. A spurious pattern of lines may appear in the detrended data, as shown, for example, in Figure 3 from *Denis et al.* [2002]. Finally, the technique should not be used for fields which are noisier at the boundaries than in the LAM interior.

[20] We now briefly review *Errico*'s [1985] method to determine the power spectra of ($a_{i,j}$) within the LAM domain with constant grid spacing and dimension $N_I \times N_J$. To remove the partially resolved spatial variability of waves beyond the scale of the domain, the data are linearly detrended along constant i, j. For example, for each j, the slope is determined:

$$s_j = \frac{a_{N_I,j} - a_{1,j}}{N_I - 1} \tag{3}$$

For each i, j the linear trend in the I direction is removed:

$$a'_{i,j} = a_{i,j} - \frac{1}{2}(2i - N_i - 1)s_j \tag{4}$$

An identical procedure is completed with i and j reversed in (1) and (2) and with $a'_{i,j}$ replacing $a_{i,j}$ in (2). The result is a detrended field $a^N_{i,j}$. The spectral coefficients ($c_{p,q}$) of $a^N_{i,j}$

are determined by the discrete two-dimensional Fourier transform:

$$c_{p,q} = \frac{1}{(N_I - 1)(N_J - 1)} \sum_{j=1}^{N_J - 1} \sum_{i=1}^{N_I - 1} a_{ij}^{N} e^{\sqrt{-1}\Delta x \varpi} \tag{5}$$

$$\varpi = p(i-1) + q(j-1) \tag{6}$$

where p and q represent zonal and meridional wavenumbers with discrete values:

$$p = \frac{2\pi l}{\Delta x} \frac{1}{N_I - 1} \qquad l = 0, \pm 1, \ldots, \pm \frac{N_I}{2} \tag{7}$$

$$q = \frac{2\pi l}{\Delta x} \frac{1}{N_J - 1} \qquad l = 0, \pm 1, \ldots, \pm \frac{N_J}{2} \tag{8}$$

The one-dimensional power spectrum (in k space) is given by

$$S(k) = \sum c_{p,q} c_{p,q}^{*} \tag{9}$$

where $c_{p,q}^{*}$ is the complex conjugate of $c_{p,q}$. The one-dimensional wave number (k) is

$$k = \left(p^2 + q^2\right)^{1/2} \tag{10}$$

Successive values of k are evenly spaced in wavenumber space by the minimum wavenumber (Δk), which is defined by the minimum fundamental wavenumber of p and q:

$$k - \frac{1}{2}\Delta k < \left(p^2 + q^2\right)^{1/2} < k + \frac{1}{2}\Delta k \tag{11}$$

The maximum wavenumber is defined by the Nyquist wavenumber of the grid:

$$k_{Nyquist} = \frac{\pi}{\Delta x} \tag{12}$$

[21] When the reanalysis data are interpolated to the RAMS oblique polar stereographic (rectangular) grid, the maximum resolved wavenumber in Cartesian space will slightly decrease with decreasing latitude. For reference, we nominally define the Nyquist wavenumber of the reanalysis here as its minimum possible value on the globe, which occurs at the equator:

$$k_{Nyquist}^{*} = 1.13 \times 10^{-5} \mathrm{m}^{-1}$$

This corresponds to a minimum resolved wavelength (λ) of approximately 550 km. Some atmospheric modeling texts, though, suggest that the minimum wavelength that has meaningful representation in a discrete model is not $2\Delta x$, but at least $4\Delta x$ [*Pielke*, 2002]. Using this definition, the wavenumber of physically resolved waves in the reanalysis is likely:

$$k_{max}^{*} = 5.65 \times 10^{-6} \mathrm{m}^{-1}$$

corresponding to a maximum wavelength of approximately 1100 km. This differentiation between $k_{Nyquist}^{*}$ and k_{max}^{*} will prove helpful in explaining the behavior of model spectra in section 3. Henceforth, k_{max}^{*} will also be used as the separation point between what is referred to as "large" ($k < k_{max}^{*}$) and "small" scale ($k > k_{max}^{*}$).

2.3. Model Variables Analyzed

[22] In this study, we investigate two atmospheric model variables ($a_{i,j}$) using the methodology just described: (1) the column average total kinetic energy ($Ek_{i,j}$), and (2) the column integrated moisture flux convergence ($MFC_{i,j}$). There are two a priori reasons for selecting these particular atmospheric variables. First, they are good diagnostic measures of the energy and moisture budgets, respectively, within the model. Second, each variable reflects different scales of atmospheric behavior. The integrated kinetic energy is principally a function of large-scale winds at upper-levels (less than 500 mbar) and so should be relatively insensitive to surface forcing. MFC, on the other hand, should be more sensitive to surface boundary forcing since water vapor rapidly decreases upward. MFC is a good proxy for rainfall and low-level vertical motion. Additionally, in spring and summer MFC on a continental scale in North America is related to a topographically forced diurnal cycle. This a priori physical understanding of the two atmospheric fields being analyzed is critical in explaining their spectral behavior in the RAMS simulations. The model-generated precipitation is also analyzed and compared to observations. As a surface field, precipitation is considered because it is one of the best observed quantities to validate RCM performance and a principle diagnostic variable used in RCM studies.

[23] The column-average total kinetic energy is computed using a stepwise integration downward through the column, divided by the pressure depth of the (model) atmosphere. For each i, j point:

$$Ek_{i,j} = \frac{1}{g\left(p_s - p_{Top}\right)} \int_{p_{Top}}^{p_s} \frac{1}{2}\left(u^2 + v^2 + w^2\right) dp \tag{13}$$

where p_s is surface pressure, p_{Top} is the pressure at the highest vertical level, and u, v, and w correspond to the zonal, meridional, and vertical wind, respectively. The domain-averaged total kinetic energy is then:

$$\overline{Ek} = \frac{\sum_{j=1}^{N_J} \sum_{i=1}^{N_I} Ek_{i,j}}{N_I N_J} \tag{14}$$

Similarly, the column integrated moisture flux convergence for each i, j point is

$$MFC_{i,j} = -\frac{1}{g} \int_{p_{Top}}^{p_s} \nabla \cdot \left(q\,\vec{v}\right) dp \tag{15}$$

[24] It is important to note that these fields are computed as a post-processing step after the model simulations are completed. None of the model variables used in the

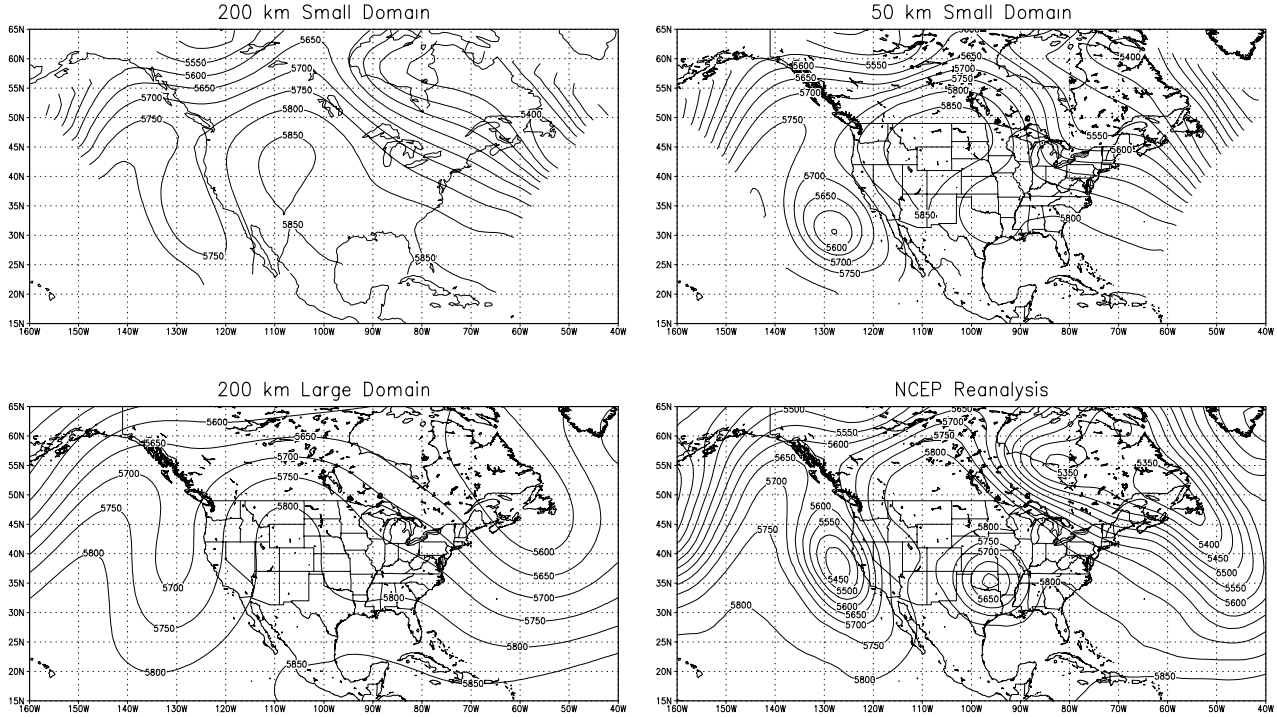

Figure 2. The 500-mbar height (m) on 0Z UTC, 12 May 1993, for indicated model basic experiments and NCEP Reanalysis.

computation of kinetic energy or MFC exhibits variability at the boundary that is significantly different from the interior, so the two-dimensional (2-D) spectral analysis procedure is justified. While the same cannot perhaps be said of precipitation, we believe the spectral analysis for that field is also justified because the area analyzed (the contiguous United States) for this variable is well within the RCM interior. The results for precipitation spectra, as will be shown later, are also physically reasonable.

[25] Once the spectrum of a given variable is computed for a particular analysis time, it is smoothed using a three-point weighted filter. This smoothing is necessary to reduce noise before comparison with different spectra. To compare the spectral power per wavenumber of the reanalysis assimilation $S(k)_{obs}$ to the model simulation $S(k)_{mod}$, the fractional change in spectral power per wavenumber is computed at each analysis time as:

$$\Delta S(k)_{frac} = \frac{S(k)_{mod}}{S(k)_{obs}} - 1 \tag{16}$$

[26] Results are presented in terms of this ratio averaged over the thirty (twice-daily) analysis times for the last fifteen days of simulation, rather than the actual spectra themselves. It is important to note that only the latter part of the simulation is analyzed, to avoid any spin-up issues and ensure the model is in a RCM mode. If the model simulation has, on average, more variability than the regridded reanalysis for a given wavenumber, the ratio will be positive, and vice versa. If $\Delta S(k)_{frac}$ is less than zero for a given value of k, than RAMS does not add any variability to $a_{i,j}$ beyond the NCEP reanalysis. For experiments described in section 3.4, in which one model simulation (mod_1) is compared to a second model simulation (mod_2) the formulation for $\Delta S(k)_{frac}$ is

$$\Delta S(k)_{frac} = \frac{S(k)_{mod_1}}{S(k)_{mod_2}} - 1 \tag{17}$$

This second formulation is useful to determine if surface information is adding value for $k > k^*_{max}$, in the absence of observed mesoscale data to validate the model against. We compare in section 3.4 the model spectra of precipitation directly to the corresponding NCEP observations (regridded to the RAMS model grid), in which case:

$$\Delta S(k)_{frac} = \frac{S(k)_{precip_{RAMS}}}{S(k)_{precip_{NCEP}}} - 1 \tag{18}$$

We present the results for $\Delta S(k)_{frac}$ in the proceeding sections on a logarithmic (base 10) scale with the corresponding wavelength scale (in m) also displayed on the plots. $\Delta S(k)_{frac}$ may appear more noisy at smaller scales, and this is expected because (1) the spectrum is more highly resolved in physical space and (2) the ratio is emphasizing very small differences between two spectra at high wavenumbers and very large differences at low wavenumbers.

3. Results

3.1. An Illustration of Simulated 500-mbar Height

[27] We select a sample model-simulated day with a highly amplified 500-mbar height field (Figure 2). This particular day is twelve days from model initialization, and it is generally illustrative of what the RAMS model produces in a Type 2 downscaling mode. Significant

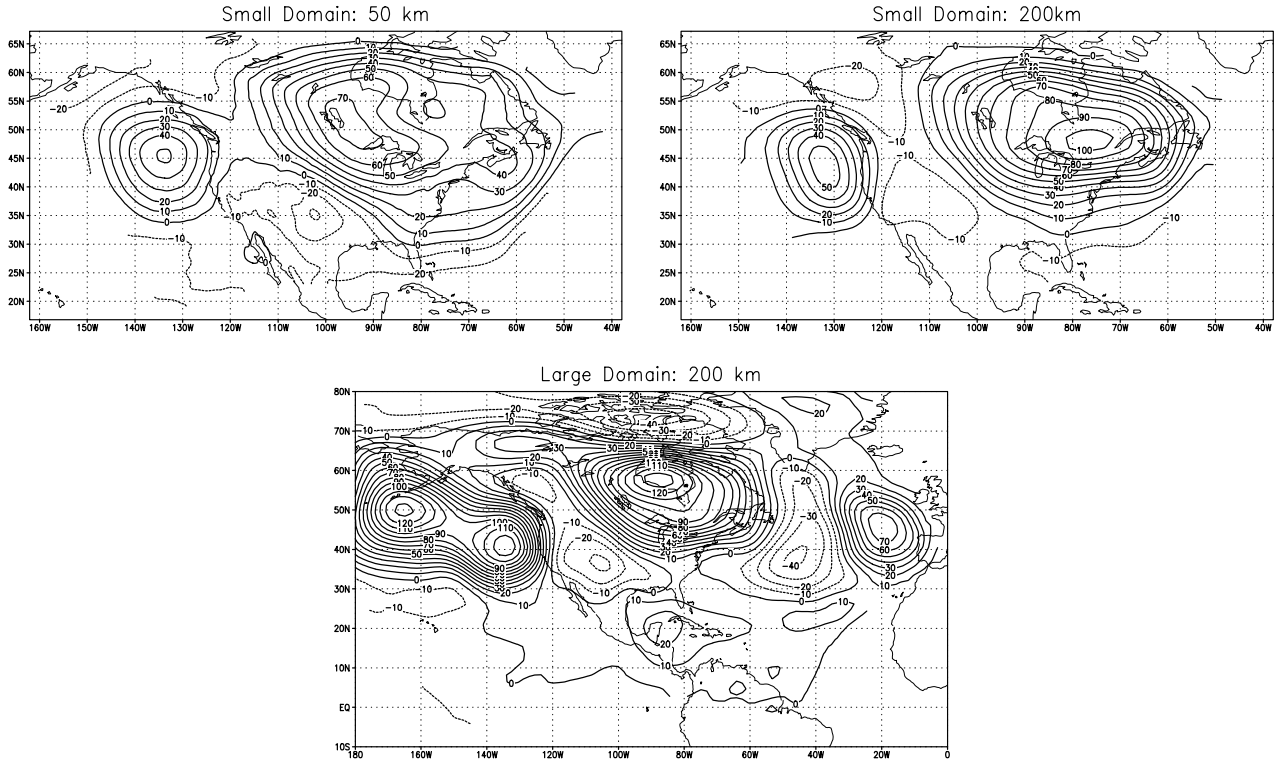

Figure 3. Average error in RAMS-simulated 500-mbar height (m) for the given model domain constraints (last 15 days of simulation). Contour interval is 10 m.

synoptic features apparent in reanalysis observations are not present in the model simulations. For example, the ridge in the central United States is too far south and west, and the cutoff lows off the California coast and in the central United States are not as strong or appear as open waves. The height field degrades with increased domain size. Such errors lead to significant differences in representation of surface fields, such as precipitation (see section 3.4). Even with the smallest domain and 50 km grid spacing, the highly amplified features are not as defined as they are in the reanalysis.

[28] To illustrate this loss of variability in 500-mbar height further, Figure 3 shows the average error in 500-mbar height for the last fifteen days of simulation for the three model domain sizes corresponding to Figure 2. The errors progressively worsen as both grid spacing increase and domain size increase, exceeding 120 m in the central North Pacific for the large 200 km domain. The greatest underestimation of mean 500-mbar height occurs in regions of low pressure troughs, such as off the west coast of North America and Europe, and the semipermanent trough near Hudson Bay. These observations indicate that RAMS is not correctly retaining value of the large-scale as given by the NCEP reanalysis. A very similar result was found by *Jones et al.* [1995] downscaling GCM data over Europe, particularly for a large RCM domain.

3.2. Two-Dimensional Spectral Analysis of Basic Experiments

[29] $\Delta S(k)_{frac}$ averaged over the last fifteen days of simulation is shown for kinetic energy and MFC for the small domain (basic experiments 1–3) in Figure 4. As previously mentioned, k in Figure 4 is presented on a logarithmic scale. k^*_{max} and $k^*_{Nyquist}$ are indicated with dashed and solid lines, respectively, for reference. We have two a priori expectations for behavior of $\Delta S(k)_{frac}$ with respect to k. First, the regional model should correctly retain value of the variability of kinetic energy and MFC present in the reanalysis data. Thus, in the region $k < k^*_{max}$ $\Delta S(k)_{frac}$ should be near zero. Second, though there is likely some aliasing of the reanalysis data to larger wavenumbers, the regridded reanalysis ($S(k)_{obs}$) should have rapidly decreasing spectral power from k^*_{max} to $k^*_{Nyquist}$ and little or no spectral power for $k > k^*_{Nyquist}$. We should then expect that $\Delta S(k)_{frac}$ should always be greater than zero in the region $k > k^*_{Nyquist}$. It is in the region $k < k^*_{max}$ where $\Delta S(k)_{frac}$ is more physically meaningful. Dissipation of kinetic energy in nature occurs at wavenumbers greater than $k^*_{Nyquist}$ and so the value of $\Delta S(k)_{frac}$ at the large scale (low wavenumbers) is due entirely to the physics of the RCM.

[30] For kinetic energy (Figure 4a), several characteristic behaviors of $\Delta S(k)_{frac}$ are independent of grid spacing. For wavenumbers below k^*_{max} ($\lambda > 1100$ km), the model underestimates the spectral power and does not retain value of the large scale. The greatest underestimation appears to be at k^*_{max} itself. This affects the development of baroclinic waves in the model, which was apparent from Figure 2. Then, as k increases towards $k^*_{Nyquist}$ and beyond, there is an increase in spectral power of the RCM compared to the regridded reanalysis. This makes sense given our a priori assumption for behavior of regridded reanalysis spectra. The increase could be due to either forcing from the surface boundary or

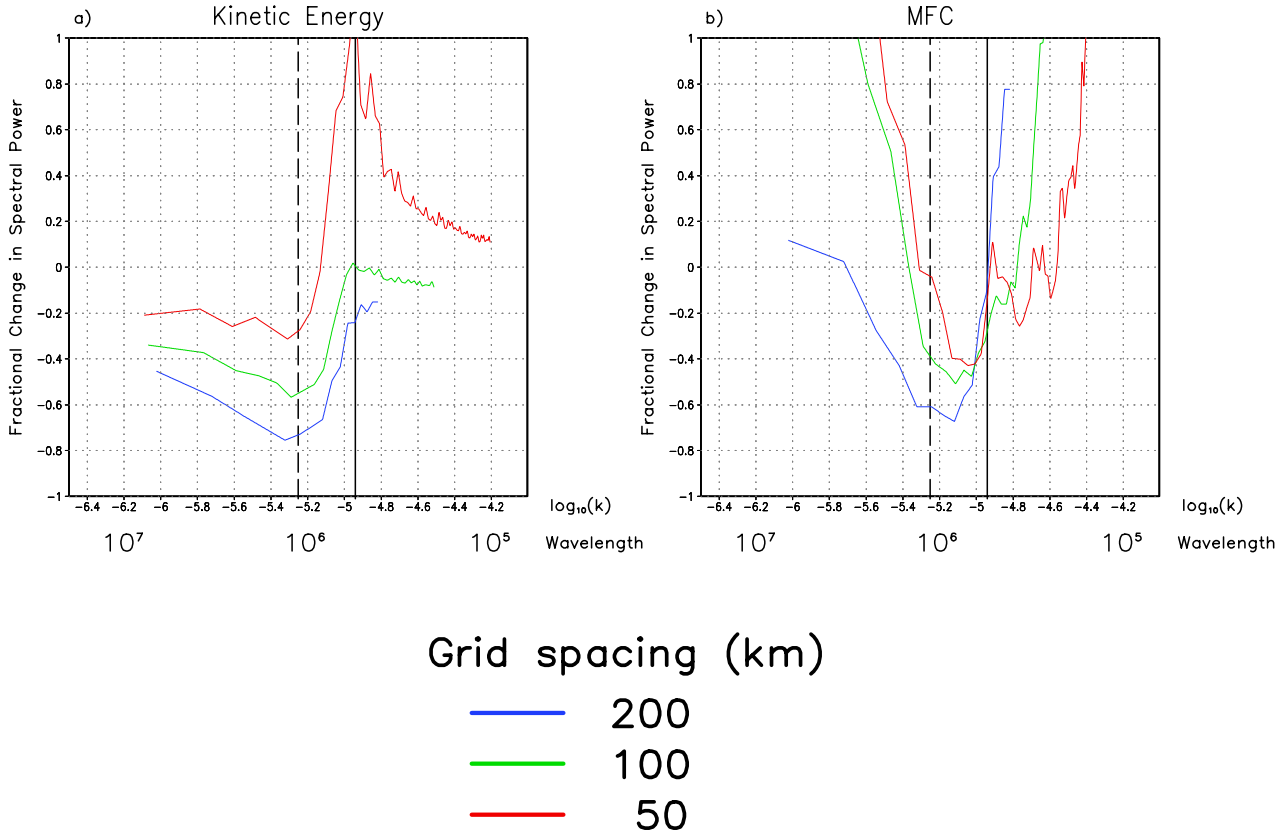

Figure 4. Fractional change in spectral power ($\Delta S(k)_{frac}$) versus $\log_{10}(k)$ and wavelength, small domain experiments for (a) column-average total kinetic energy and (b) column integrated moisture flux convergence (MFC). The dashed black line indicates k^*_{max}, and the solid black line indicates $k^*_{Nyquist}$. k in units of m^{-1}. Wavelength in units of m.

local hydrodynamic instabilities. For the 50 km simulation, as k increases RAMS begins to add value to kinetic energy ($\Delta S(k)_{frac} > 0$) at a point between k^*_{max} and $k^*_{Nyquist}$ and continues to add value thereafter. Similar behavior is also observed for MFC as k increases, (Figure 4b) with a low value of $\Delta S(k)_{frac}$ near k^*_{max} and an increase near $k^*_{Nyquist}$ and beyond.

[31] Changes in the grid spacing and domain size also have characteristic responses in $\Delta S(k)_{frac}$. As grid spacing increases, $\Delta S(k)_{frac}$ decreases for $k < k^*_{max}$. For the 200 km or 100 km grid spacing small domain run (basic experiments 1 and 2), $\Delta S(k)_{frac}$ for kinetic energy does not exceed zero for any value of k. Though we should expect $\Delta S(k)_{frac}$ to be greater than zero beyond $k^*_{Nyquist}$, it is not for the larger domains. In these cases RAMS is not adding any information beyond the noise present in the regridded reanalysis. The same general behavior is also observed for MFC (Figure 4b). $\Delta S(k)_{frac}$ does exceed zero for the very largest of scales, though much of the variability of MFC and rainfall occurs at smaller scales. The larger domain (kinetic energy shown in Figure 5) exhibits identical behavior as the small domain, except that the loss in $\Delta S(k)_{frac}$ at large scales, with the exception of the 200 km grid spacing simulation, is worse than for the corresponding small domain experiments at the same grid spacing. The underestimation of variability at larger scales dramatically affects how the RCM adds value at the smaller scale ($k > k^*_{max}$), and this will be shown for RCM-generated precipitation in section 3.4.

3.3. Time Evolution of Model Simulated to Regridded Reanalysis Kinetic Energy

[32] The time evolution of the fraction of model simulated to regridded reanalysis domain averaged total kinetic energy ($\overline{Ek}$) is shown in Figure 6 for the six basic experiments. $\overline{Ek}$ should be very well reflected by the regridded reanalysis since, as mentioned, it mostly reflects the upper-level horizontal winds at scales large scales. Regardless of grid spacing or grid size, the ratio of model simulated to regridded reanalysis $\overline{Ek}$ in all of the simulations decreases in time, on average. It is closer to the reanalysis kinetic energy at certain times when the flow is more zonal. This decrease is particularly pronounced during approximately the first few days of RCM simulation, then gradually levels off. For the small grid, 50 km grid spacing simulation (basic experiment 3), approximately 85% of the regridded reanalysis $\overline{Ek}$ is preserved after 30 days of simulation, but over 30% is lost for the 200 km grid spacing simulation (basic experiment 1). As the grid spacing for the small domain increases, the loss of kinetic energy worsens. Shown also in Figure 6 are the same results for the area of the large domain within the small domain (dotted curves). Considering the same area in all the simulations, the loss in kinetic energy

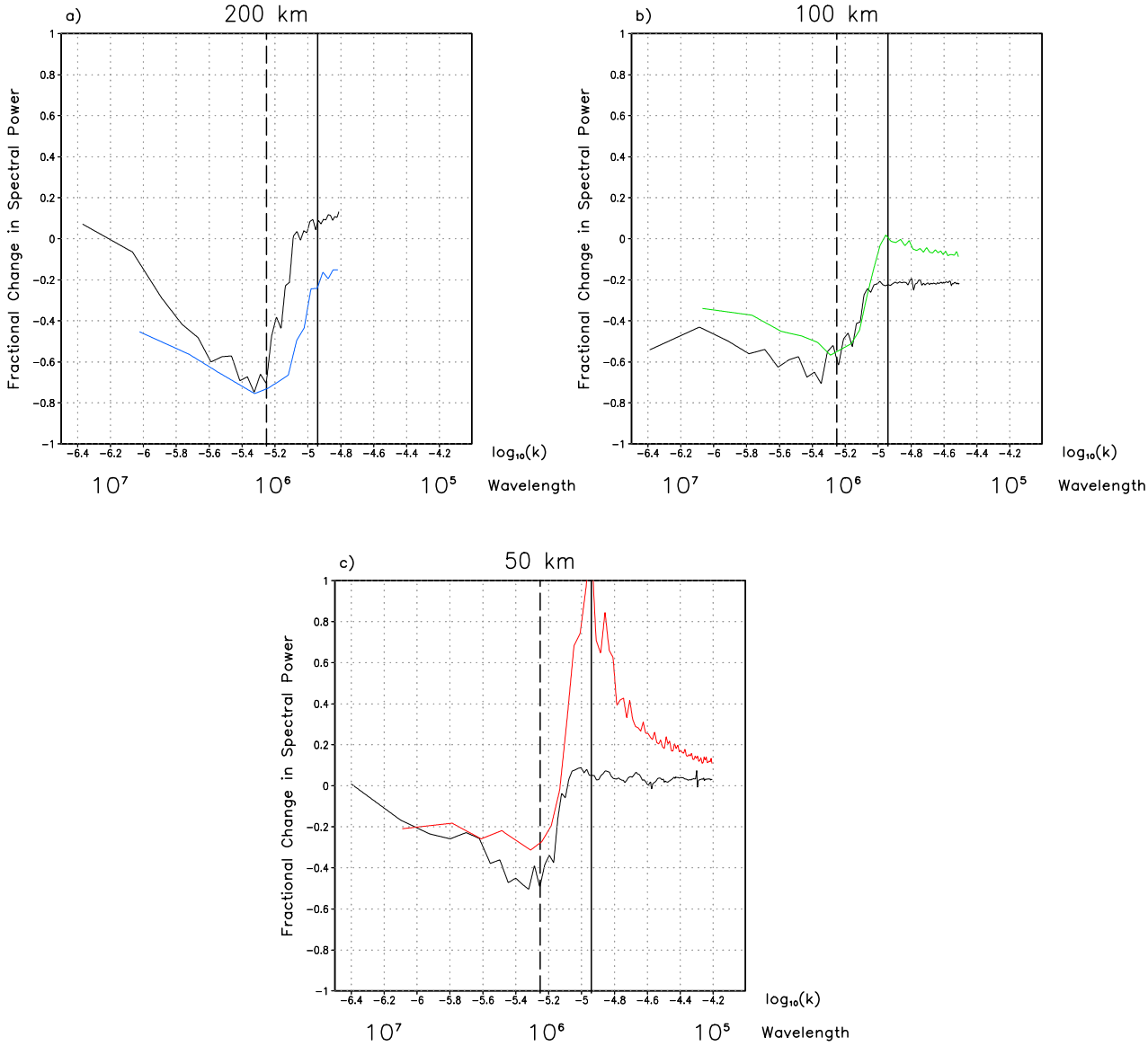

Figure 5. Fractional change in spectral power ($\Delta S(k)_{frac}$) versus $\log_{10}(k)$ for column-average total kinetic energy, small and large domain experiments: (a) Δx = 200 km, (b) Δx = 100 km, and (c) Δx = 50 km. Small domain experiments color-coded as in Figure 4, and large domain experiments shown as corresponding solid black curve. The dashed black line indicates k^*_{max}, and the solid black line indicates $k^*_{Nyquist}$. k in units of m^{-1}. Wavelength in units of m.

also worsens with increased domain size. For the 200 km grid spacing large domain, the model underestimates the observed kinetic energy by nearly 50% after thirty days of simulation. The reasons for this loss in kinetic energy, and solutions to alleviate it, will be discussed in section 4.

[33] Additionally, Figure 7 shows the time evolution of the fraction of model simulated to reanalysis regridded domain-averaged kinetic energy variance ($\bar{\sigma}^2_{EK}$). It is very similar to Figure 6. The model underestimates $\bar{\sigma}^2_{EK}$ for all grid spacings. In general, as the domain size gets larger and the grid spacing increases, the underestimation of $\bar{\sigma}^2_{EK}$ worsens, though there are specific days that are exceptions. In a mean sense, this underestimation also worsens as time proceeds, irrespective of grid spacing or domain size. The periods where $\bar{\sigma}^2_{EK}$ is most underestimated are times where the synoptic pattern is highly amplified; it is better estimated at times of more zonal flow. At the end of the simulation period, $\bar{\sigma}^2_{EK}$ is underestimated by the model in the range of approximately 10-30% for the small domain. A similar result is shown by *von Storch et al.* [2000, Figure 5] considering the meridional winds simulated by the regional climate model REMO with only lateral boundary forcing.

3.4. Additional Follow-On Experiments

[34] Four additional follow-on experiments were performed to investigate the effect of internal nudging (Follow-on 1); a larger grid (Follow-on 2); a change in the convective parameterization (Follow-on 3); and a

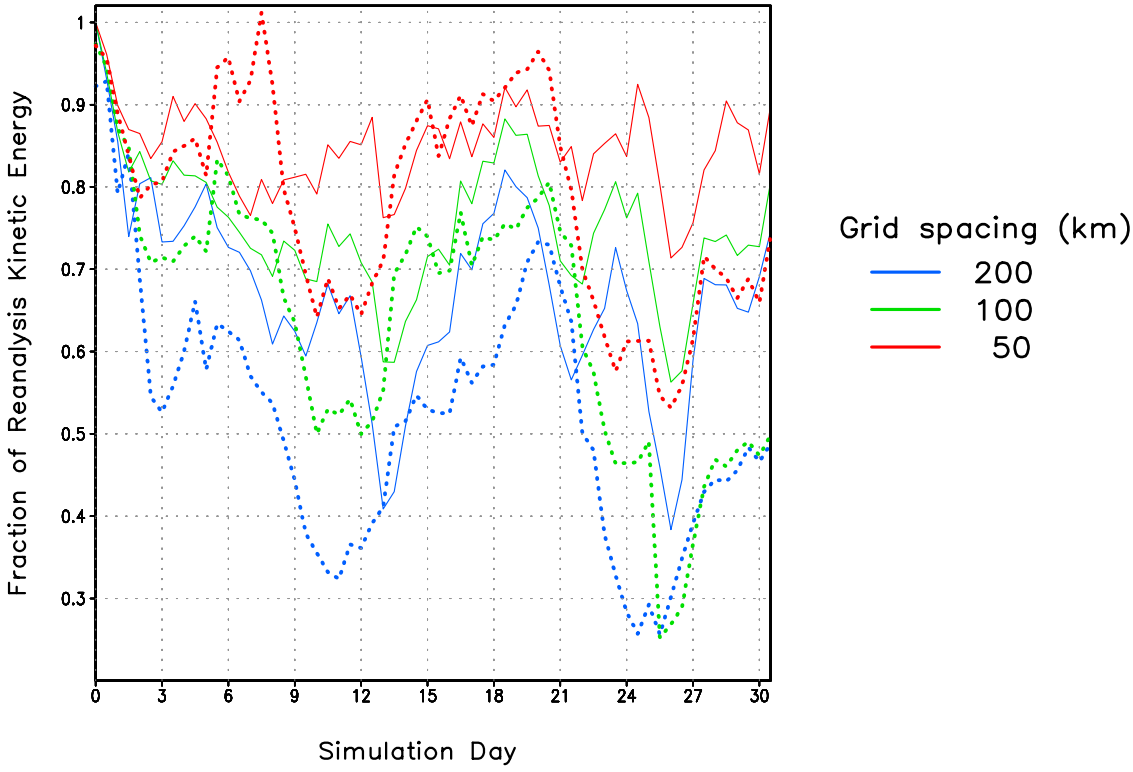

Figure 6. Time evolution of the fraction of model simulated to reanalysis regridded domain-averaged total kinetic energy for the six basic experiments on equivalent grids. The small domain is indicated by a solid curve, and the large domain is indicated by a dashed curve.

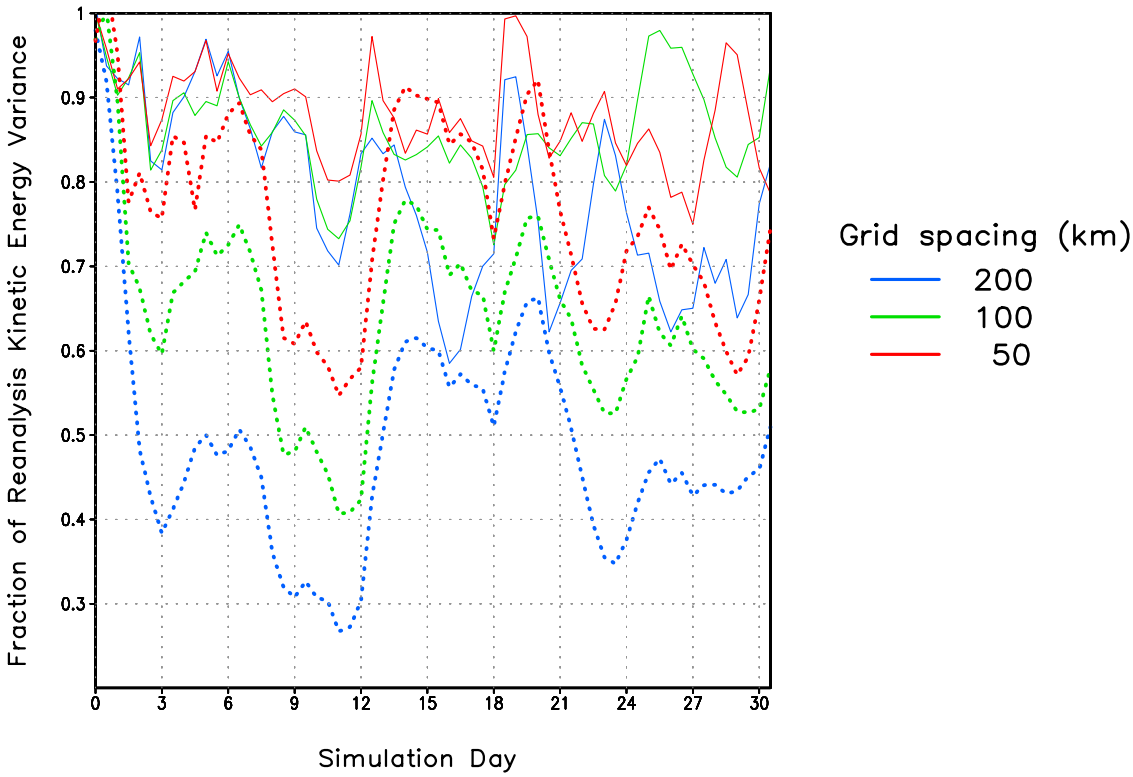

Figure 7. Same as Figure 6 for model domain-averaged kinetic energy variance.

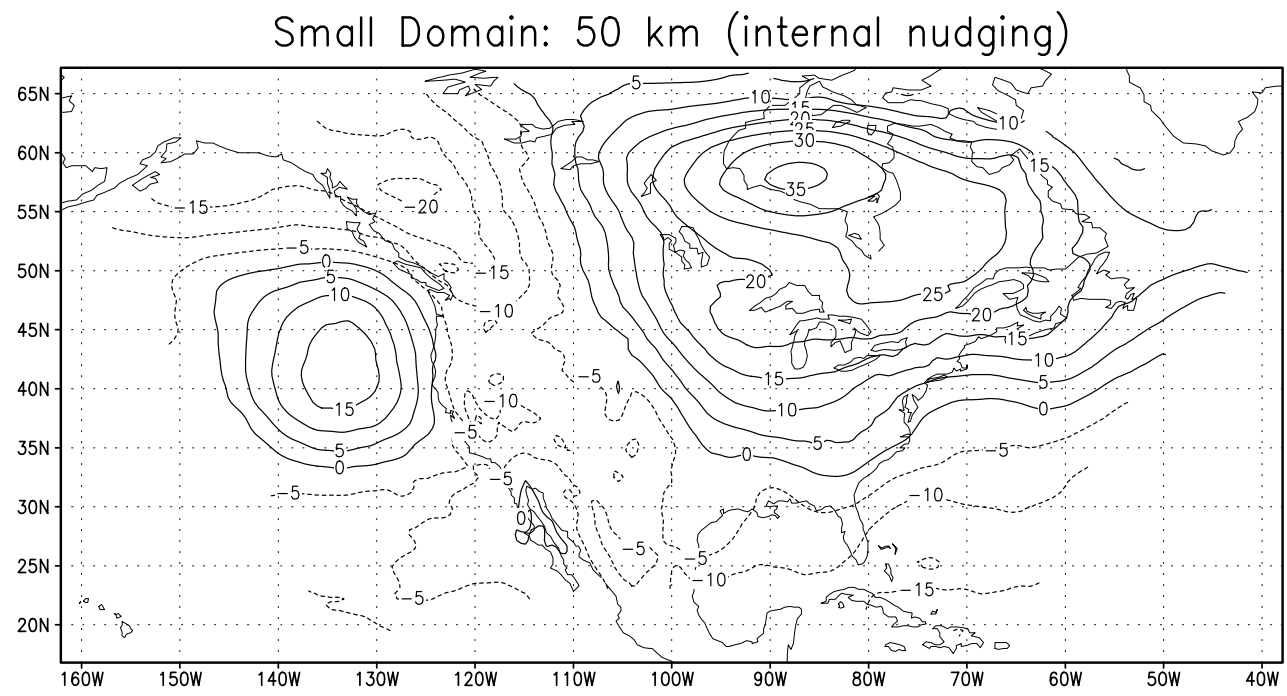

Figure 8. Same as Figure 3 for Follow-on 1 (internal nudging). Contour interval is 5 m.

homogeneous surface boundary (Follow-on 4). These were performed using the grid of basic experiment 3 (50 km, small domain) because that maintained the best fidelity with the reanalysis. In Follow-on 1, internal nudging on a one-day timescale was activated. To put this in perspective, according to the RAMS Users Guide, internal nudging at an hourly timescale corresponds to "very strong nudging." The RAMS Users Guide recommends an internal nudging timescale of two to four hours for the typical RAMS simulation with a short-term model integration (less than a day), multiple nested grids, and explicit treatment of microphysics. Our timescale for internal nudging is considerably larger and exactly what is used in real-time forecast application with a continental-scale domain in South America (P. L. Silva Dias, personal communication). In Follow-on 2, the model domain of the smaller grid is extracted from the larger one in basic experiment 6. Follow-on 3 uses the Kain-Fritch convection scheme, in lieu of the Kuo scheme, with and without internal nudging. In Follow-on 4, the model was run using flat topography, a constant sea surface temperature (295 K), a single vegetation type (mixed cropland), and a single soil type (sandy clay loam). This experiment serves as a control run to see how the characteristic behavior of $\Delta S(k)_{frac}$ is influenced by the variable surface boundary, principally the topography. These additional experiments are designed to assess the value added by RAMS for small scales ($k > k^*_{max}$).

[35] For Follow-on experiments 1–3 we use equation (17) for computation of $\Delta S(k)_{frac}$, where mod_1 is the follow-on experiment and mod_2 corresponds with basic experiment 3. Since we are now comparing model to model results, $\Delta S(k)_{frac}$ is physically meaningful for all k, even greater than k^*_{max}. A positive value of $\Delta S(k)_{frac}$ in this case means the model generated variability is greater than the basic experiment, and vice versa.

[36] The monthly average difference in 500-mbar height from observations for Follow-on 1 (internal nudging) is shown in Figure 8. Compared to basic experiment 3 shown in Figure 3 earlier, the same pattern of error appears, but the magnitudes are less. This shows internal nudging, as would be expected, is improving the model representation of the large scale. $\Delta S(k)_{frac}$ for kinetic energy and MFC are shown for Follow-on 1 in Figure 9. With internal nudging activated, variability of kinetic energy wavenumbers less than k^*_{max} does improve, and, therefore, lessens the loss in kinetic energy with time as observed in Figure 6. We note there is still some loss of kinetic energy compared to the reanalysis, but it is not as large as that for the no-nudge case shown in Figure 4. However, by imposing a strong constraint on the interior of the domain, the variability of kinetic energy is decreased for wavenumbers greater than k^*_{max}. For MFC, $\Delta S(k)_{frac}$ is negative for all k. The decrease in variability at high wavenumbers means that the small-scale features are diminished in strength when internal nudging is activated. In their work with RAMS, *Weaver et al.* [2002] similarly found internal nudging weakened mesoscale motions and lead to stronger turbulence in a shallower boundary layer. For example, Figure 10 shows the comparison values of monthly precipitation for the small domains using lateral boundary nudging only and with interior nudging on the small domain. In the nudged run, precipitation throughout the domain is reduced, particularly in the central and eastern United States. Figure 10 also shows the precipitation for Follow-on 2 and Follow-on 4, which will be discussed later. For Follow-on 2, precipitation is substantially increased in regions of significant topography.

[37] The precipitation results for Follow-on 2 (large-domain) in Figure 10 would imply that the weaker the influence of the larger-scale forcing of the reanalysis, the

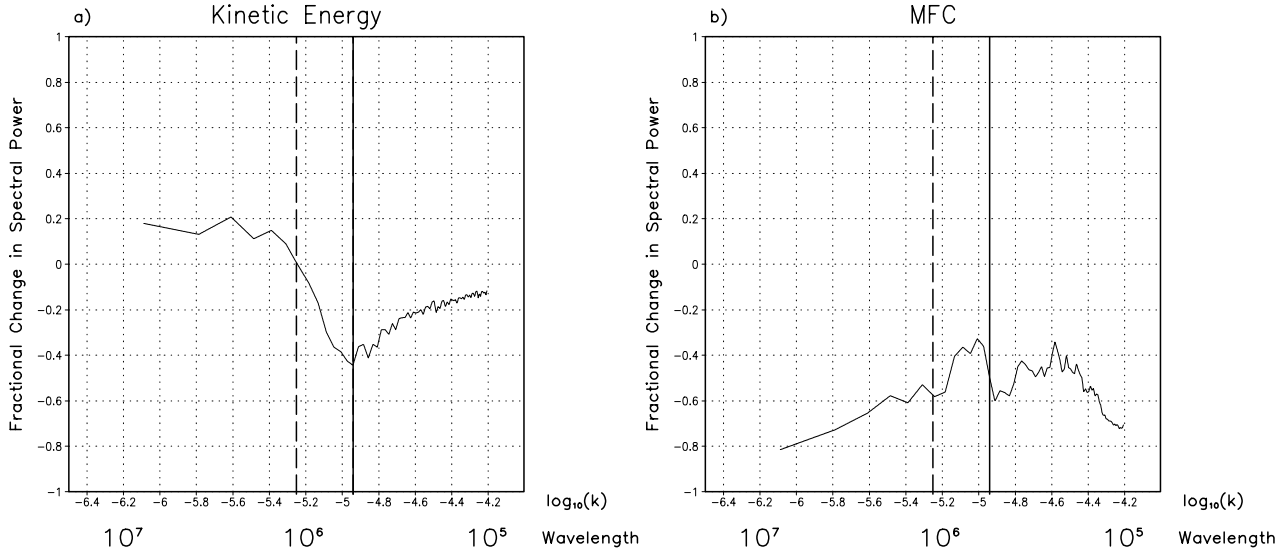

Figure 9. Average fractional change in spectral power ($\Delta S(k)_{frac}$) versus $\log_{10}(k)$ and wavelength for (a) column-averaged kinetic energy and (b) column integrated moisture flux convergence (MFC), Follow-on 1 (internal nudging). The dashed black line indicates k^*_{max}, and the solid black line indicates $k^*_{Nyquist}$. k in units of m^{-1}. Wavelength in units of m.

greater control the surface boundary conditions exert on the vertical motion and distribution of precipitation. The behavior of RAMS in this respect would be identical to other mesoscale models [e.g., *Jones et al.*, 1995, 1997; *Jacob and Podzun*, 1997; *Seth and Giorgi*, 1998]. For Follow-on 2, the ratio of the spectra of the large (extracted) domain (mod_1) to the small domain (mod_2) was computed using equation (17), and these are shown in Figure 11. Increasing the domain size reduces the variability of kinetic energy for all k, and this should be expected given the results already seen. However, $\Delta S(k)_{frac}$ for MFC is greater than zero for $k > k^*_{max}$. We show later in Follow-on 4 that the mechanism which is enhancing variability of MFC at that scale is the topography.

[38] Use of the KF convective parameterization scheme (Follow-on 3) markedly changes the model-generated precipitation, as shown in Figure 12 along with the corresponding NCEP 0.25° gauge observations [*Higgins et al.*, 1996]. The KF scheme produces more precipitation in the simulation domain than the Kuo scheme, whether internal nudging is activated or not. The KF scheme in RAMS generally overestimates precipitation in areas of steep, elevated terrain. A terrain-adjusted trigger function can alleviate this problem [*Castro et al.*, 2002]. In Figure 13, changing the convection scheme does not change the kinetic energy for $k < k^*_{max}$. It does modestly increase the kinetic energy (by about 20%) beyond k^*_{max}. The variability in MFC is much larger, particularly for $k > k^*_{max}$. In this range, the KF scheme is more than doubling the variability of MFC. In the KF simulations, the stronger MFC variability is explained by the enhanced rainfall. Over the length of a RCM simulation, the use of a different convection scheme may dramatically effect the surface energy and moisture budget of the model and, hence, surface feedback to the atmosphere.

[39] The question, however, is to determine, with respect to precipitation, which particular model setup yields the best result in terms of the NCEP observations shown in Figure 12. Given that these are Type 2 dynamical downscaling simulations, it is reasonable to expect that the RCM should reproduce (in a gross sense) the day-to-day climate variability on weekly and longer timescales. An evaluation of model performance against observations defines the model skill. Precipitation results are considered for four different RAMS experiments: Kuo with no interior nudging (basic experiment 3), Kuo with interior nudging (Follow-on 1), KF with no interior nudging, and KF with interior nudging (Follow-on 3). Considering the last fifteen days of simulation, a spatially varying correlation coefficient was determined using daily precipitation totals. The square of the correlation coefficient yields the spatially averaged explained variance of model precipitation to observations. The difference in monthly precipitation from the NCEP observations along with the domain-averaged bias and explained variance are shown in Figure 14. Though fifteen days of data are insufficient to generate a statistically significant signal, they are nonetheless good enough show the biases associated with each convection scheme and how interior nudging changes the explained variance of precipitation in the model domain.

[40] The Kuo scheme underestimates the precipitation in the central United States and overestimates in regions of steep terrain gradients, such as occurs in the Rocky Mountains or Appalachians. Though the bias in the no interior nudging case is the smallest of the simulations considered (−7.50 mm), the domain-averaged explained variance of precipitation is the lowest of the simulations considered in Figure 14 (9.7%). The domain-average explained variance is about the same for Follow-on 2 (large domain), but precipitation biases associated with terrain are enhanced (not shown). When the entire month is considered, the explained variance for the large-domain experiment is lower than that of the small domain. This suggests that better representation of the large scale in the smaller domain experiment improves

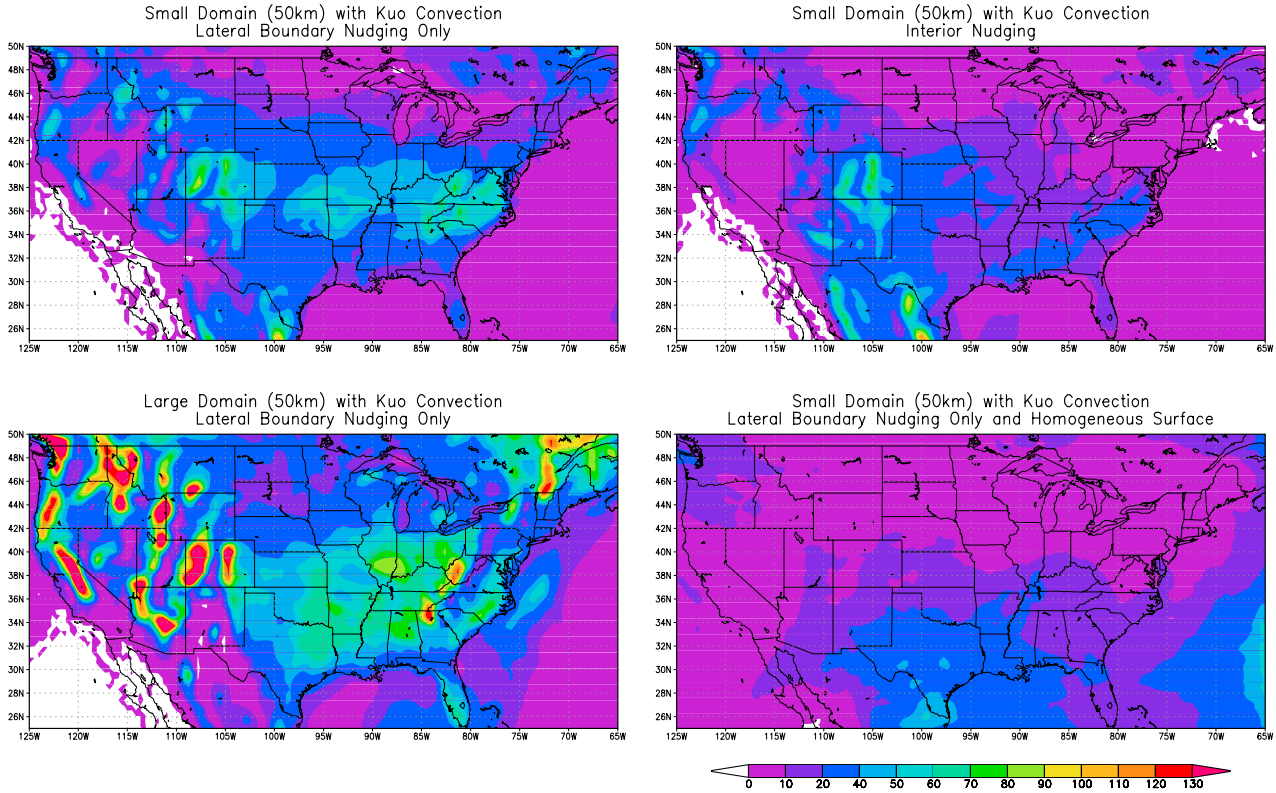

Figure 10. RAMS-simulated convective precipitation with the Kuo scheme for model constraints indicated. Period considered is last 15 days of simulation. Precipitation in mm.

the RAMS model-generated precipitation. When interior nudging is applied, the underestimation of the Kuo scheme worsens in the central United States (a domain-average bias of −16.79 mm). The explained variance of daily precipitation increases (to 16.7%). Even though precipitation is more underestimated when interior nudging is applied, its spatial distribution is closer to observations.

[41] Considering the KF simulation absent internal nudging, precipitation is generally overestimated everywhere with a large positive domain-averaged bias (45.85 mm). The problem with excessive precipitation in steep terrain gradients is magnified. The KF simulation with interior nudging greatly improves the precipitation error in the central and eastern United States. However, the problem with high precipitation in the mountains still exists, and therefore there is a high bias in precipitation (18.75 mm). As with the Kuo scheme, the simulation with interior nudging yields a better domain-averaged explained variance.

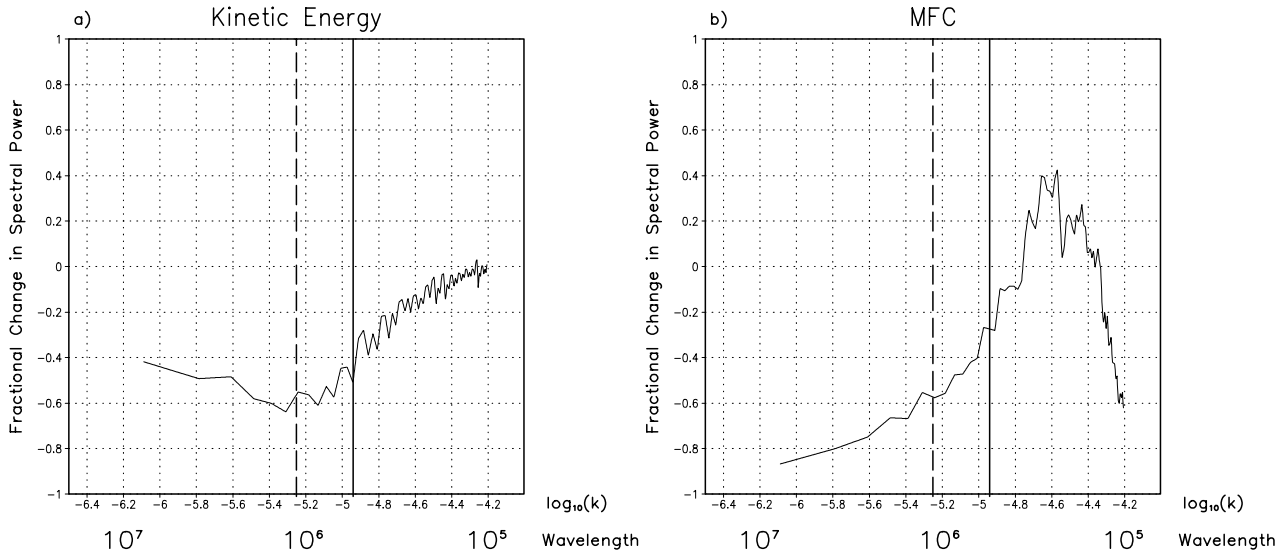

Figure 11. Same as Figure 9 for Follow-on 2 (larger grid).

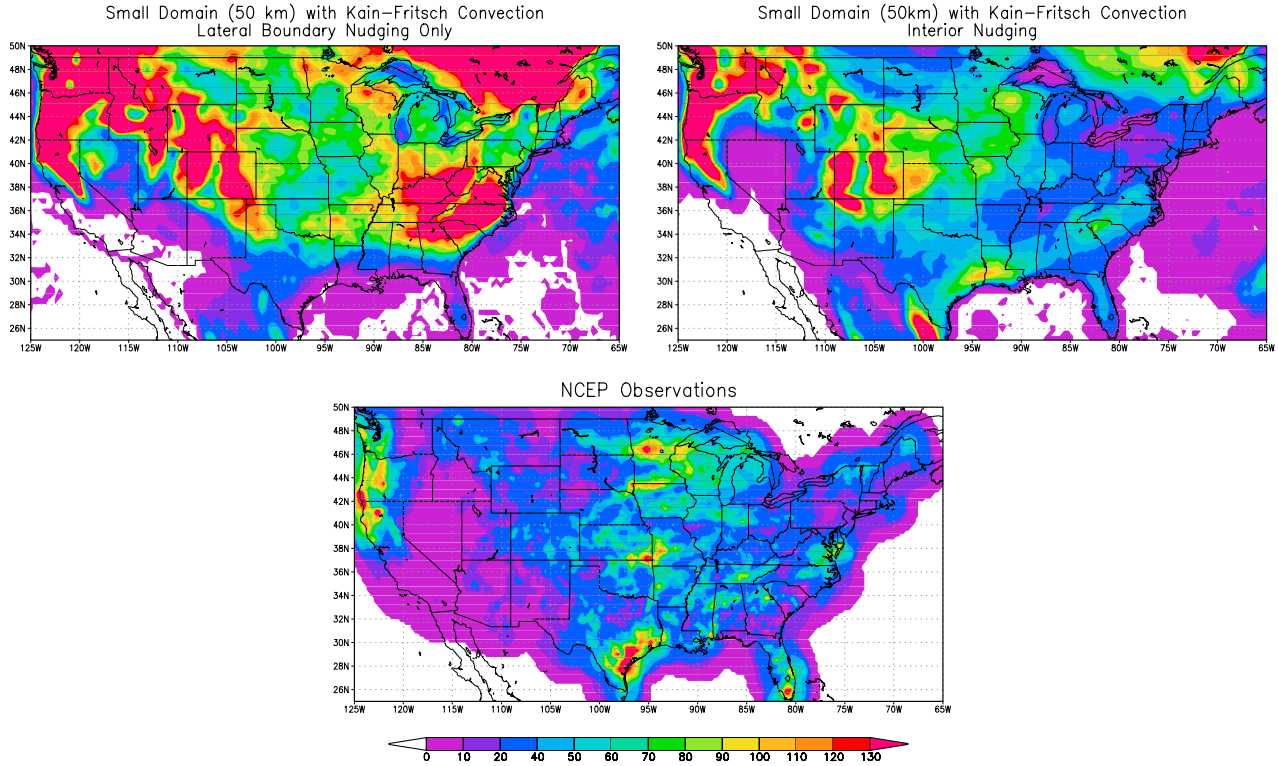

Figure 12. RAMS-simulated convective precipitation with the Kain-Fritsch scheme for model constraints indicated and observed precipitation from NCEP. Period considered is last 15 days of simulation. Precipitation in mm.

[42] How does the spectral behavior of model-generated precipitation correspond to observations for these four simulations in Figure 14? Figure 15 shows $\Delta S(k)_{frac}$ of the RAMS precipitation compared to the NCEP observations following equation (18). The Kuo scheme, whether internal nudging is applied or not, underestimates the observed spatial variability at all scales. For the KF runs, variability is enhanced, particularly at the larger scales, because of the pattern of precipitation bias associated with the terrain in the western United States. The best representation of the spatial variability of NCEP observations is captured by the KF scheme with internal nudging. At the small scale, the spatial variance of the KF generated precipitation from the nudged run and the NCEP observed precipitation is roughly identical. Therefore, though the Kuo scheme has a lower-domain averaged bias, the Kain-Fritsch scheme with internal nudging does the superior job of representing the spatial distribution and variability of

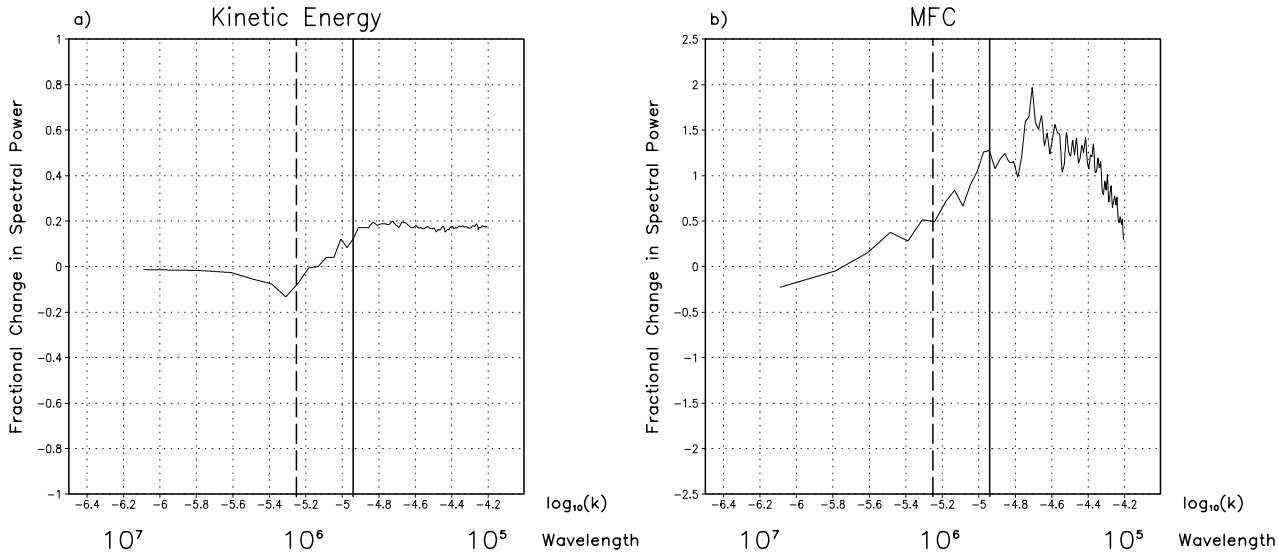

Figure 13. Same as Figure 9 for follow-on experiment 3 (Kain-Fritsch convection).

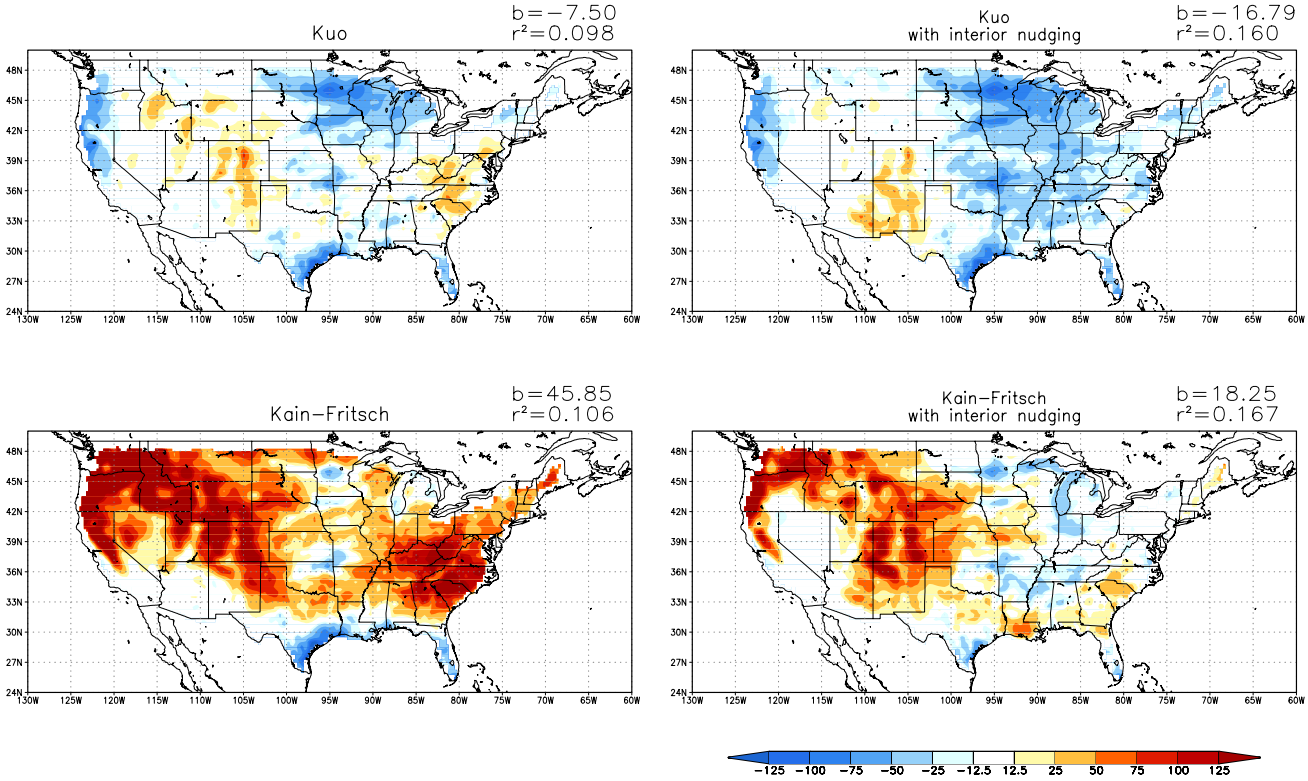

Figure 14. Difference between RAMS-simulated precipitation and NCEP observed precipitation (mm) over the contiguous United States for the model conditions specified. Domain-averaged bias and explained variance (r^2) included. Period considered is last 15 days of simulation.

precipitation in RAMS for this particular month of May 1993.

[43] Finally, Follow-on 4 (homogeneous surface boundary experiment) serves as a control to evaluate the impact of topographic forcing. The precipitation for this experiment is included in Figure 10. Compared to the other experiments with the Kuo scheme, there is little precipitation in the western United States associated with the topography, as

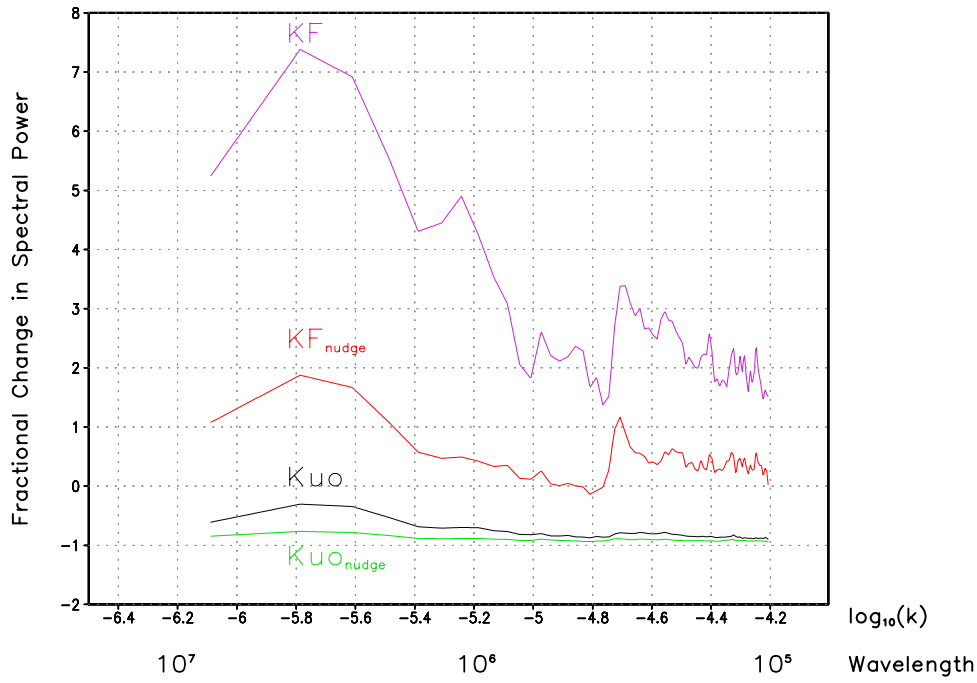

Figure 15. Fractional change in spectral power ($\Delta S(k)_{frac}$) versus $\log_{10}(k)$ and wavelength for different RAMS-generated model precipitation solutions on the 50 km small domain grid. k in units of m^{-1}. Wavelength in units of m.

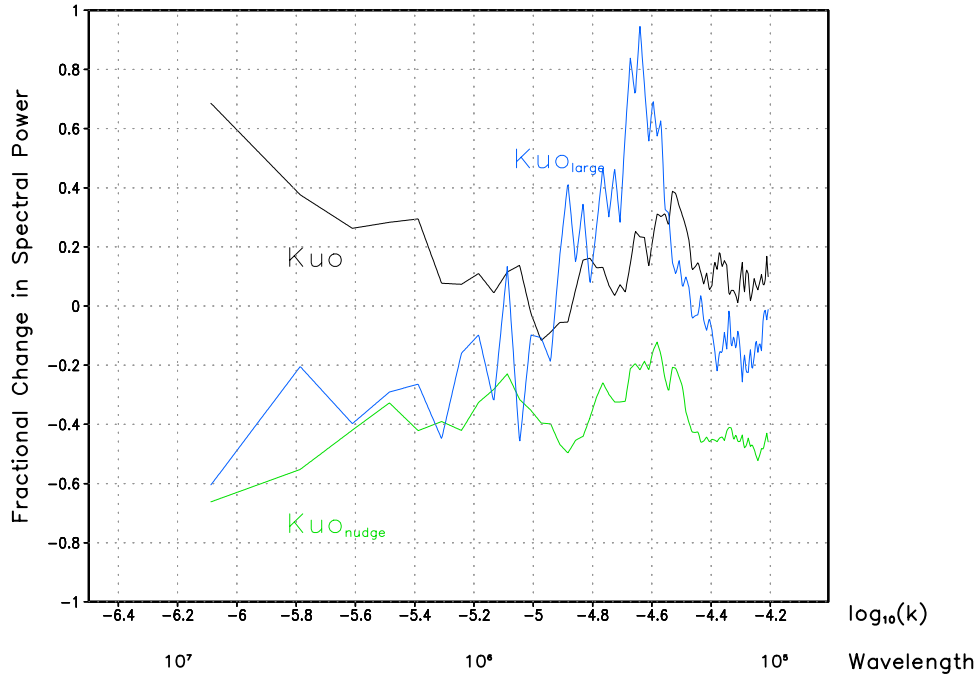

Figure 16. Fractional change in spectral power ($\Delta S(k)_{frac}$) versus $\log_{10}(k)$ and wavelength, experiments with the Kuo scheme compared to Follow-on 4. The quantity considered is the MFC multiplied by the topographic gradient in the model. k in units of m^{-1}. Wavelength in units of m.

would be expected. There is also less precipitation in the central and eastern United States, in areas of relatively homogeneous terrain. Because spring and summer precipitation is tied to a diurnal cycle of convection forced by the topography, eliminating the topography alters the precipitation distribution across the entire continent. In the evaluation of $\Delta S(k)_{frac}$, since the integrated kinetic energy has little relationship to surface forcing, we omit analysis of it here and focus exclusively on MFC. Also, instead of evaluating the MFC on its own, we first multiply it by the topographic gradient in the model and then perform the two-dimensional spectral analysis described in section 2. In this way, the relationship between the topography and MFC can be evaluated. We perform this analysis on Follow-on 4 (*mod 2*) as the control experiment against which all other previous experiments with the 50 km small domain are evaluated (*mod 1*) using equation (17). For these experiments, $\Delta S(k)_{frac}$ is interpreted as follows: if greater than zero, the topography contributes to the variability in MFC at a given value of k beyond what its variability would be with no topography; if less than zero, it does not.

[44] Figure 16 shows $\Delta S(k)_{frac}$ for the experiments with the Kuo scheme (experiments labeled in the plot). For these experiments, the largest positive value for $\Delta S(k)_{frac}$ occurs at approximately $\lambda \sim 250$ km for the large domain experiment. A similar, though weaker, peak appears for the smaller domain, confirming that the increase in MFC variability in Figure 11 is indeed due to increased sensitivity to the topography when the domain is enlarged. In the run with internal nudging, though, $\Delta S(k)_{frac}$ is always below zero, so the topography does not contribute to the variability of MFC beyond the model simulation with no topography. This does not necessarily imply, though, that the topography is not contributing to the variability of MFC in this particular simulation. Its influence is just weaker. Recalling the pattern of precipitation bias in Figure 14, this likely explains why the precipitation in the Kuo simulation, with internal nudging especially, underestimates the precipitation in the central and eastern United States. This convective precipitation is due to a topographically forced diurnal cycle of MFC which is underestimated by the model in that particular configuration.

[45] For the experiments with the KF scheme (Figure 17), we see similar behavior to the Kuo experiments. Topography enhances MFC at the same preferential scale, and the peak in $\Delta S(k)_{frac}$ exceeds zero for the simulations in which nudging is and is not applied. In spite of the internal nudging for the KF case, the topography is able to add information to the RCM and influence the diurnal cycle of MFC. Hence, we observe the improvement in the spatial variability of precipitation in the KF internally nudged simulation described earlier. This provides further evidence that the choice of (convective) parameterization schemes seriously affects how the surface boundary adds information to the RCM.

4. Discussion

[46] Absent interior nudging, the RAMS model in RCM mode will have greater error at larger scales as both horizontal grid spacing and domain size increase. This error is due to the failure of the RCM to correctly retain value of the large scale, which is particularly acute at the limit of physically resolved waves in the larger global model (k^*_{max}). For the typical RCM setup in which a continental-scale domain is used, with a grid spacing less than 50 km, the underestimation of kinetic energy over a month of simulation may be tolerable and barely noticeable (less than 5%).

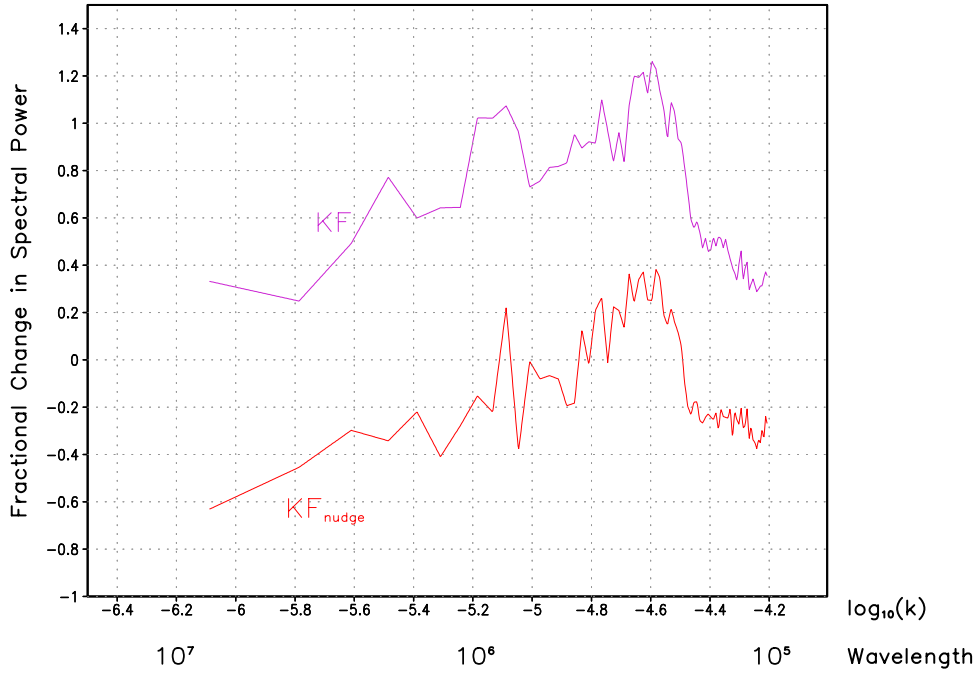

Figure 17. Same as Figure16 for experiments with the KF scheme.

However, when the RAMS model was applied to a very large domain or a coarse grid spacing ($\Delta x > 50$ km) on a continental-scale domain is used, kinetic energy was underestimated for all k. RAMS does add value for k greater than k^*_{max} especially if there is sufficient surface boundary forcing, such as variations in topography, and that forcing can be resolved by the model. The sensitivity to the surface forcing increased when the model domain size increased, as shown by analysis of the integrated moisture flux convergence. Though the focus here was on topography, presumably similar effects may occur for any variable surface field, like vegetation, soil moisture, or snow cover. We also observed that changing the model convective parameterization scheme increased the sensitivity to the surface boundary.

[47] The first important question raised in the current study is what causes the loss of large-scale kinetic energy with time, absent interior nudging to the RCM? The most obvious answer would seem to be the parameterized horizontal diffusion. As seen in Table 6, because of the dependence on grid spacing, the lower limit of the diffusion coefficient will increase by about an order of magnitude from a 50 km to 200 km simulation. This increase in diffusion is necessary for numerical stability. The loss of kinetic energy is a well known problem of global models, and can be directly linked to diffusion. We attempted to reduce the user-specified parameters (C_x and K_A) used in diffusion computation to their minimum values as suggested by the RAMS Users Guide, but this did not mitigate the kinetic energy loss. There is also the likely possibility that, in addition to horizontal diffusion some or all of the other one-dimensional column parameterizations are insufficient to retain value of the large scale. These would include the parameterizations for convection and/or cloud microphysics, radiation, and subgrid-scale mixing.

[48] As an example, let us consider the simulation of large-scale precipitation in addition to a convective parameterization scheme. Accounting for large-scale precipitation allows for supersaturation through explicit uplift of moisture. The resulting heating increases the buoyancy of uplifted air and enhances its upward vertical motion, providing a mechanism for conversion of potential to kinetic energy. Reliance entirely on the convection scheme can also suppress large-scale vertical motions by increasing static stability and further reduce the energy conversion. An additional simulation (50 km, small grid) was executed with a full cloud microphysical representation of large-scale precipitation. $\Delta S(k)_{frac}$ was computed according to equation (16), and the results are shown in Figure 18. For comparison, $\Delta S(k)_{frac}$ from Figure 4 (the simulation with only the convection scheme) is included for reference. Accounting for the large-scale precipitation decreases the loss of kinetic energy at the large scale, but does not eliminate it. At k^*_{max} the loss decreases from approximately 30% to 10%. Beyond k^*_{max} the variability of kinetic energy is substantially increased over using the convection scheme alone. In spite of the better representation of large-scale energy, though, the domain-averaged precipitation for this simulation is overestimated and its spatial pattern is poor compared to observations (not shown).

[49] The second important question is why there seems to be a change in trend in $\Delta S(k)_{frac}$ at k^*_{max}. For $k < k^*_{max}$ there is always a kinetic energy loss compared to the reanalysis, irrespective of grid size or grid spacing. For $k > k^*_{max}$, this loss either decreases in magnitude or the RCM begins to add value. Would there be a similar dependence of k^*_{max} on $\Delta S(k)_{frac}$ irrespective of the resolution of the GCM or reanalysis? If so, then it would possible to determine a priori which wavelengths the RCM would tend to degrade, absent some interior nudging technique.

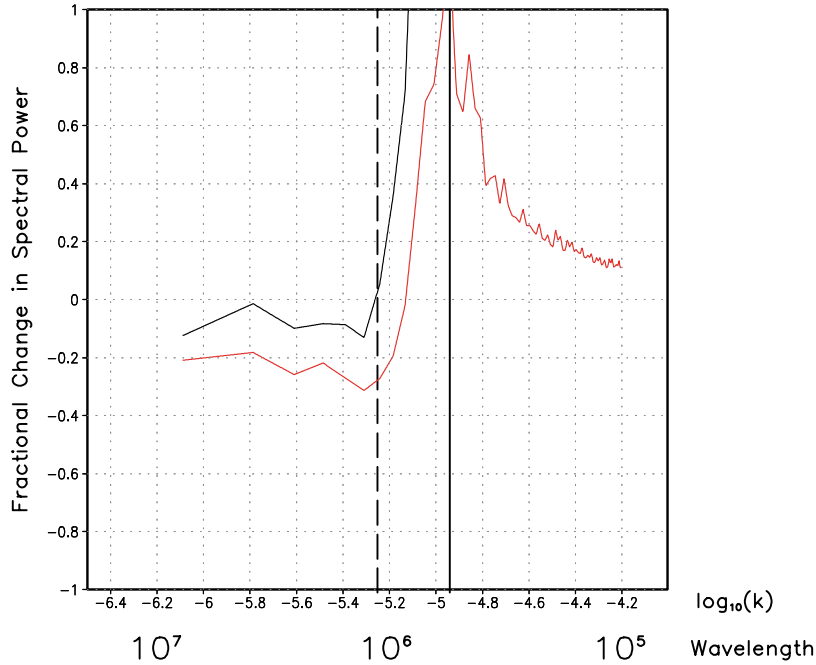

Figure 18. Fractional change in spectral power ($\Delta S(k)_{frac}$) versus $\log_{10}(k)$ and wavelength, for column-average total kinetic energy. The red curve is the basic experiment 3 simulation (convection scheme only), and the black curve is the same simulation with convection and explicit microphysics. The dashed black line indicates k^*_{max}, and the solid black line indicates $k^*_{Nyquist}$. k in units of m^{-1}. Wavelength in units of m.

[50] Is there a way to alleviate the large-scale kinetic energy loss shown in Figure 6 and yet preserve the value added by the RCM at the small scale? Simply increasing the number of nudging points would seem to be a solution, but we found exactly the same loss of kinetic energy when the number of nudging points was increased to ten. The albeit crude, four-dimensional data assimilation technique of internal nudging may be applied, as demonstrated in Figure 9. The results in Figure 9 are really nothing new and should not be surprising in light of the results from studies using a variety of other RCMs over the past decade [e.g., *von Storch et al.*, 2000; *Sasaki et al.*, 1995; *Giorgi et al.*, 1993b; *Kida et al.*, 1991]. These studies conclude that improvement in RCM simulation can be achieved by selective nudging of the large-scale, or a spectral nudging technique. This is probably the best solution. G. Miguez-Macho et al. (Spectral nudging to improve dowscaling over North America using the Regional Atmospheric Modeling System (RAMS), submitted to *Journal of Climate*, 2003) recently demonstrated the utility of a spectral nudging technique for RAMS (not yet incorporated in the standard release of the model). Using a domain very similar to the small domain used here, they found a large improvement in the June 2000 precipitation over the central United States solely due to spectral nudging of the large-scale (defined as $\lambda > 2500$ km) throughout the entire depth of the troposphere.

[51] Internal nudging such as we have used here, in which all wavelengths are relaxed to the reanalysis solution, we acknowledge, is far less desirable. In agreement with *Weaver et al.* [2002], we found interior nudging tends to weaken small-scale variability. This small-scale variability may not only arise from the presence of topography, but purely via local hydrodynamic variability. Examples include frontogenesis, development of convective cloud bands, and hurricane intensification. None of these examples requires surface inhomogeneities for their development and none is resolvable on the reanalysis grid. Absent detailed mesoscale data or regional reanalyses, there is no way to quantify what the value added may be. Weak internal nudging at a long timescale may still preserve some of the small scale variability because most it occurs at a diurnal timescale or less. For example, with the KF scheme in RAMS, the internally nudged solution yields the model representation of precipitation, in terms of spatial distribution and variability. Aside of areas of significant topography in western North America, some areas of relatively homogeneous topography, such as in the central and eastern United States, also exhibited a low precipitation bias in the KF simulation in which internal nudging was applied.

[52] What is really advocated with the use of spectral nudging, or interior nudging for that matter, is the introduction of some method of large-scale closure needed by the LAM when run as a RCM. The use of spectral nudging would retain the kinetic energy of the large-scale and let the large-scale forcing reinitialize the fine-scale domain during the model integration period. In the absence of four-dimensional data assimilation, however, in order to retain the kinetic energy requires that the model dynamics and physics, as we have previously defined, generate the energy. As we have already demonstrated, the one-dimensional forms of the parameterized model physics are unable to generate enough kinetic energy to retain that of the reanalysis. This issue is likely endemic to all RCMs, since each use similar dynamic and physical representations.

[53] To test this hypothesis, we suggest this experiment (or similar) be repeated with other RCMs to demonstrate

whether this behavior exists. If this is the case, it implies that only applying lateral boundary nudging using a *Davies* [1976] nudging or similar technique is insufficient for RCMs. A universal alternative needs to be implemented. Previous work, with RAMS and other models, shows the best alternative is a spectral nudging technique. The evidence presented here suggests the domain should be nudged for $k < k^*_{max}$, where k^*_{max} is dependent on the resolution of the forcing data. Because there is such a large sensitivity to the RCM experimental design, when comparing results from different models it is necessary to ensure they use the same grid size, grid spacing, and nudging options in order to accurately assess the RCM-generated small scale variability.

[54] The results here also challenge the traditional notion of a grid setup for RCM dynamical downscaling. RAMS was originally designed for simulation of short-term weather events on a cloud-resolving scale. Recall that "short term" is defined as a time scale of days to a couple of weeks. For these Type 1 experiments, a multiple nesting paradigm is typically followed. The coarsest grid has the same approximate horizontal scale as the reanalysis or global model (Δx = 100–250 km). Within the coarsest grid, there is an intermediate nested (mesoscale) grid (Δx = 10–50 km). Finer nested grid(s) (Δx < 10 km) may be added to capture specific weather events, if so desired. There are two reasons for such a model setup. First, it has been assumed inappropriate to assimilate the reanalysis or global model data at a scale much smaller than $k^*_{Nyquist}$. Second, it is typically computationally prohibitive to run a cloud-resolving simulation for a very large grid. There have been recent advances in computing power so that this may be come widely feasible in the near future, though. The multiple grid nesting approach works because the model retains a large sensitivity to the initial conditions. For example, even after a week of simulation the 200 km grid spacing small domain still preserves approximately 80% of the reanalysis assimilated kinetic energy.

[55] The results here, though, suggest the multiple grid nesting paradigm may not yield the most desirable results when RAMS (or any other RCM) is run in a RCM mode. A coarse grid of Δx = 100–200 km may introduce undesirable weakening of large-scale atmospheric variability for a model integration exceeding two weeks or so. A better strategy may be to assimilate the reanalysis directly to the mesoscale grid (a single grid paradigm). The global model or reanalysis data is then driving the RCM for the scale in which it retains value of the large scale. Bypassing the coarser grid may also (1) save computing resources, and (2) avoid the problem of using different parameterization schemes, such as for convection, on different grids which may introduce additional uncertainties in model simulation results [e.g., *Gochis et al.*, 2002]. However, caution must be taken not to have too large a ratio of GCM grid spacing to LAM grid spacing. The RAMS Users Guide suggests that if this ratio exceeds a value of six, reflections may occur at the lateral boundaries due to grid disparities.

5. Summary

[56] In this study, the value retained and added by dynamical downscaling has been quantitatively evaluated by considering the spectral behavior of RAMS in relation to its domain size and grid spacing. To do this, a RAMS-RCM simulation was compared with a regridded reanalysis at each model analysis time for a set of six basic experiments. At large scales, RAMS cannot restore the variability present in the global model forcing data, and this loss is particularly acute at the limit of the global model physically resolved waves. As the grid spacing increases or domain size increases, the underestimation of variability at large scales worsens. The model simulated to regridded reanalysis kinetic energy exhibits a logarithmic decrease with time, which is more pronounced with larger grid spacing. This underestimation of kinetic energy is not only linked to the parameterized horizontal diffusion, but all the other one-dimensional column parameterizations in the model. The results here and past studies suggest the only solution to alleviate this problem is to constrain the RCM with the large-scale model (or reanalysis) values.

[57] Additional follow-on experiments investigated the effect of internal nudging, enlarging the domain, the use of a different convective parameterization, and a homogeneous surface boundary. These were designed mainly to investigate the value added by RAMS at the small scale. Weak internal nudging, as currently implemented in RAMS, did improve the representation of the large-scale features, but weakened the variability at small scales. The surface boundary forcing appeared to be the dominant factor in generating variability for small-scale features and exerts greater control on the RCM solution as the influence of lateral boundary conditions diminish. Changing the convection scheme increased the variability on the small scale and improved the model generated precipitation. The influence of the surface boundary forcing, then, is highly dependent on the model experimental design, such as domain size, nudging options, specification of the surface boundary itself, and model parameterization schemes. Further studies are, of course, necessary to confirm whether these behaviors apply in general to all RCMs, but previous work suggests they do. We believe it would be a very worthwhile exercise to repeat these experiments with an assortment of different RCMs, especially those which use a spectral nudging technique.

[58] These RAMS simulations are of a Type 2 framework, assuming a perfect model, so the same conclusions will apply to RAMS-RCM applications with greater degrees of freedom (Types 3 and 4). A good example for these latter types is that of *Jones et al.* [1995] that demonstrated similar results and conclusions for RCM simulations over Europe. We find for this particular case, dynamical downscaling with RAMS does not retain value of the large scale over and above that which exists in the larger global model or reanalysis. If the variability of synoptic features is underestimated or there is a consistent bias in the larger model, no increased skill would be gained by dynamical downscaling with RAMS. The utility of the RAMS-RCM, then, is not to add increased skill to the large scale, rather the value added is to resolve the smaller-scale features which have a greater dependence on the surface boundary.

[59] **Acknowledgments.** This research was funded by NOAA grant NA17RJ1228 Amendment 6, NASA grant NGT5-30344, and DOD cooperative agreement DAAD19-02-2-0005. The authors wish to thank Dallas Jean Staley for help in article preparation.

References

Bell, J. D., and J. E. Janowiak (1995), Atmospheric circulation associated with the Midwest floods of 1993, *Bull. Am. Meteorol. Soc.*, *76*, 681–695.

Black, T. J. (1994), The new NMC mesoscale Eta model: Description and forecast examples, *Weather Forecasting*, *9*, 265–278.

Castro, C. L., W. Y. Y. Cheng, A. B. Beltrán, C. H. Marshall Jr., R. A. Pielke Sr., and W. R. Cotton (2002), The incorporation of the Kain-Fritsch cumulus parameterization scheme in RAMS with a terrain-adjusted trigger function, paper presented at Fifth RAMS Users and Related Applications Workshop, Santorini, Greece.

Chen, Q.-S., and Y.-H. Kuo (1992), A harmonic-sine series expansion and its application to partitioning and reconstruction problems in a limited area, *Mon. Weather Rev.*, *120*, 91–112.

Cotton, W. R., et al. (2003), RAMS 2001: Current status and future directions, *Meteorol. Atmos. Phys.*, *82*, 5–29.

Davies, H. C. (1976), A lateral boundary formulation for multi-level prediction models, *Q. J. R. Meteorol. Soc.*, *102*, 405–418.

de Elía, R., R. Laprise, and B. Denis (2002), Forecasting skill limits of nested limited-area models: A perfect-model approach, *Mon. Weather Rev.*, *130*, 2006–2023.

Denis, B., J. Côté, and R. Laprise (2002), Spectral decomposition of two-dimensional atmospheric fields on limited area domains using the Discrete Cosine Transform (DCT), *Mon. Weather Rev.*, *130*, 1812–1829.

Denis, B., R. Laprise, J. Côté, and D. Caya (2003), Downscaling ability of one-way nested regional models: The big-brother experiment, *Clim. Dyn.*, *18*, 627–646.

Eastman, J. L., M. B. Coughenour, and R. A. Pielke Sr. (2001), The effects of CO_2 and landscape change using a couple plant and meteorological model, *Global Change Biol.*, *7*, 797–815.

Errico, R. M. (1985), Spectra computed from a limited area grid, *Mon. Weather Rev.*, *113*, 1554–1562.

Giorgi, F., M. R. Marinucci, and G. T. Bates (1993a), Development of a second-generation regional climate model (RegCM2). Part I: Boundary-layer and radiative transfer processes, *Mon. Weather Rev.*, *121*, 2794–2813.

Giorgi, F., M. R. Marinucci, and G. T. Bates (1993b), Development of a second-generation regional climate model (RegCM2). Part II: Convective processes and assimilation of lateral boundary conditions, *Mon. Weather Rev.*, *121*, 2814–2832.

Gochis, D. J., W. J. Shuttleworth, and Z. L. Yang (2002), Sensitivity of the modeled North American monsoon system regional climate to convective parameterization, *Mon. Weather Rev.*, *130*, 1282–1298.

Grell, G. A., J. Dudhia, and D. Stauffer (1994), A description of the fifth generation Penn State/NCAR mesoscale modeling system (MM5), *NCAR Tech. Note NCAR/TN-397+STR*, 117 pp., Natl. Cent. for Atmos. Res., Boulder, Colo.

Higgins, R. W., J. E. Janowiak, and Y.-P. Yao (1996), A gridded hourly precipitation database for the United States (1963–1993), *NCEP Clim. Predict. Cent. Atlas 1*, 46 pp., Natl. Cent. for Environ. Predict., Camp Springs, Md.

Houghton, J. T., , Y. Ding, D. J. Griggs, M. Noguer, P. J. van der Linden, and D. Xiaosu (Eds.) (2001), *Climate Change 2001: The Scientific Basis—Contribution of Working Group I to the Third Assessment Report of the Intergovernmental Panel on Climate Change* (*IPCC*), 944 pp., Cambridge Univ. Press, New York.

Jacob, D., and R. Podzun (1997), Sensitivity studies with the regional climate model REMO, *Meteorol. Atmos. Phys.*, *63*, 119–129.

Jones, R. G., J. M. Murphy, and M. Noguer (1995), Simulation of climate change over Europe using a nested regional-climate model. I: Assessment of control climate, including sensitivity to location of lateral boundaries, *Q. J. R. Meteorol. Soc.*, *121*, 1413–1449.

Jones, R. G., J. M. Murphy, M. Noguer, and A. B. Keen (1997), Simulation of climate change over Europe using a nested regional-climate model. I: Comparison of driving and regional model responses to a doubling of carbon dioxide, *Q. J. R. Meteorol. Soc.*, *123*, 265–292.

Kain, J. S., and J. M. Fritsch (1993), Convective parameterization for mesoscale models: The Kain-Fritsch scheme, in *The Representation of Cumulus Convection in Numerical Models*, *Meteorol. Monogr.*, vol. 24, pp. 165–170, Am. Meteorol. Soc., Boston, Mass.

Kalnay, E., et al. (1996), The NCEP/NCAR 40-year reanalysis project, *Bull. Am. Meteorol. Soc.*, *77*, 437–471.

Kida, H., T. Koide, H. Sasaski, and C. Masaru (1991), A new approach for coupling a limited area model to a GCM for regional climate simulations, *J. Meteorol. Soc. Jpn.*, *69*, 723–728.

Kuo, H. L. (1974), Further studies of the parameterization of the influence of cumulus convection on large-scale flow, *J. Atmos. Sci.*, *31*, 1232–1240.

Laprise, R. (2003), Resolved scales and nonlinear interactions in limited-area models, *J. Atmos. Sci.*, *60*, 768–779.

Liston, G. E., and R. A. Pielke Sr. (2001), A climate version of the Regional Atmospheric Modeling System, *Theor. Appl. Climatol.*, *68*, 155–173.

Mahrer, Y., and R. A. Pielke Sr. (1977), A numerical study of the airflow over irregular terrain, *Contrib. Atmos. Phys.*, *50*, 98–113.

Mellor, G. L., and T. Yamada (1974), A hierarchy of turbulence closure models for planetary boundary layers, *J. Atmos. Sci.*, *31*, 1791–1806.

Mesinger, F., T. L. Black, and M. E. Baldwin (1997), Impact of resolution and of the Eta coordinate on skill of the Eta model precipitation forecasts, in *Numerical Methods in Atmospheric and Oceanic Modeling*, edited by C. Lin, R. Laprise, and H. Ritchie, pp. 399–423, Andre J. Robert Mem. Monogr. Soc., NRC Res. Press, Ottawa, Ont., Canada.

Molinari, J. (1985), A general form of Kuo's cumulus parameterization, *Mon. Weather Rev.*, *113*, 1411–1416.

Pielke, R. A., Sr. (2001), Earth system modeling—An integrated assessment tool for environmental studies, in *Present and Future of Modeling Global Environmental Change: Toward Integrated Modeling*, edited by T. Matsuno and H. Kida, pp. 311–337, Terra Sci., Tokyo.

Pielke, R. A. Sr. (2002), *Mesoscale Meteorological Modeling*, 2nd ed., 676 pp., Elsevier, New York.

Pielke, R. A., Sr. et al. (1992), A comprehensive meteorological modeling system—RAMS, *Meteorol. Atmos. Phys.*, *49*, 69–91.

Reynolds, R. W., and T. M. Smith (1994), Improved global sea surface temperature analyses using optimal interpolation, *J. Clim.*, *7*, 929–948.

Sasaki, H., K. Hedji, T. Koide, and C. Masaru (1995), The performance of the long-term integrations of a limited area model with the spectral coupling method, *J. Meteorol. Soc. Jpn.*, *73*, 165–181.

Seth, A., and F. Giorgi (1998), The effects of domain choice on summer precipitation simulation and sensitivity in a regional climate model, *J. Clim.*, *11*, 2698–2712.

Smagorinsky, J. (1963), General circulation experiments with the primitive equations. Part I, The basic experiment, *Mon. Weather Rev.*, *91*, 99–164.

Takle, E. S., et al. (1999), Project to Intercompare Regional Climate Simulations (PIRCS): Description and initial results, *J. Geophys. Res.*, *104*, 19,443–19,461.

Tatsumi, Y. (1986), A spectral limited-area model with time dependent lateral boundary conditions and its application to a multi-level primitive equation model, *J. Meteorol. Soc. Jpn.*, *64*, 637–663.

von Storch, H., H. Langenberg, and F. Feser (2000), A spectral nudging technique for dynamical downscaling purposes, *Mon. Weather Rev.*, *128*, 3664–3673.

Weaver, C. P., S. B. Roy, and R. Avissar (2002), Sensitivity of simulated mesoscale atmospheric circulations resulting from heterogeneity to aspects of model configuration, *J. Geophys. Res.*, *107*(D20), 8041, doi:10.1029/2001JD000376.

Xue, M., K. K. Droegemeier, and V. Wong (2000), The Advanced Regional Prediction System (ARPS)—A multi-scale nonhydrostatic atmospheric simulation and prediction model. Part I: Model dynamics and verification, *Meteorol. Atmos. Phys.*, *75*, 161–193.

Xue, M., K. K. Droegemeier, V. Wong, A. Shapiro, K. Brewster, F. Carr, D. Weber, Y. Liu, and D. Wang (2001), The Advanced Regional Prediction System (ARPS)—A multi-scale nonhydrostatic atmospheric simulation and prediction tool. Part II: Model physics and applications, *Meteorol. Atmos. Phys.*, *76*, 143–146.

C. L. Castro, R. A. Pielke Sr., and G. Leoncini, Department of Atmospheric Science, Colorado State University, Fort Collins, CO 80523, USA. (chris@atmos. colostate.edu)